

2016

The Influence of Sea-Level Rise on Salinity in the Lower St. Johns River and the Associated Physics

Teddy Mulamba

University of North Florida, n00817214@unf.edu

Follow this and additional works at: <https://digitalcommons.unf.edu/etd>



Part of the [Civil Engineering Commons](#), and the [Other Civil and Environmental Engineering Commons](#)

Suggested Citation

Mulamba, Teddy, "The Influence of Sea-Level Rise on Salinity in the Lower St. Johns River and the Associated Physics" (2016). *UNF Graduate Theses and Dissertations*. 714.
<https://digitalcommons.unf.edu/etd/714>

This Master's Thesis is brought to you for free and open access by the Student Scholarship at UNF Digital Commons. It has been accepted for inclusion in UNF Graduate Theses and Dissertations by an authorized administrator of UNF Digital Commons. For more information, please contact [Digital Projects](#).
© 2016 All Rights Reserved

THE INFLUENCE OF SEA-LEVEL RISE ON SALINITY IN THE LOWER ST. JOHNS
RIVER AND THE ASSOCIATED PHYSICS

by

Teddy Mulamba

A Thesis submitted to the Department of Civil Engineering

in partial fulfillment of the requirements for the degree of

Master of Science in Civil Engineering

UNIVERSITY OF NORTH FLORIDA

COLLEGE OF COMPUTING, ENGINEERING AND CONSTRUCTION

December, 2016

Unpublished work c Teddy Mulamba

The Thesis titled "Influence of Sea-Level Rise on Salinity in The Lower St Johns River and The Associated Physics" is approved:

Dr. Don T. Resio, PhD

Dr. Peter Bacopoulos, PhD

Dr. William Dally, PhD, PE

Accepted for the School of Engineering:

Dr. Murat Tiryakioglu, PhD, CQE
Director of the School of Engineering

Accepted for the College of Computing, Engineering, and Construction:

Dr. Mark Tumeo, PhD, PE
Dean of the College of Computing, Engineering, and Construction

Accepted for the University:

Dr. John Kantner, PhD
Dean of the Graduate School

DEDICATION

I dedicate my thesis with the utmost gratitude to my loving parents for their continued support and encouragement. You have never missed the opportunity to remind me that I can do all things through Christ who gives me strength. I appreciate your many sacrifices and hope that this milestone will make you both very proud. To my boys: Eebs, Goyo and Pete, very few are as fortunate as I am, to be blessed with brothers I also call my best mates. Many thanks for speaking words of wisdom into my life when I needed them most. I thank God for you all every day. May we continue to live with the goal of glorifying His great name.

ACKNOWLEDGEMENTS

The completion of this thesis would not have been made possible absent the assistance and valuable contributions received from a number of people, to whom I feel obliged to express my gratitude. Principally, my utmost appreciation to Dr. Peter Bacopoulos, who I have had the pleasure of both knowing and working with for several years. His generosity, guidance and unfailing support were intricate in the completion of this study. I could not have done this without you, Sir. I truly appreciate my committee chair Dr. Don Resio, Professor and Director of the Taylor Engineering Research Institute (TERI), whose efforts made it possible for me to pursue and complete a master's degree at the University of North Florida. I am grateful for the positive learning environment you provided me with, and I consider myself very fortunate to have been one of your students. In addition, I would like to thank Dr. William Dally for agreeing to serve on my master's thesis committee, and for his noteworthy and challenging courses that have equipped me with valuable knowledge pertaining to the Coastal Engineering field. Lastly, special thanks go to Mrs. Hollis Klein, the unsung hero of the Coastal Engineering department at UNF. I, along with the rest of the graduate students, wholeheartedly appreciate everything you do on our behalf. This study was funded by the Taylor Engineering Research Institute (TERI).

TABLE OF CONTENTS

CHAPTER 1: INTRODUCTION	1
CHAPTER 2: LITERATURE REVIEW	3
2.1. Existing knowledge of the lower St. Johns River	3
2.2. Sea-level rise impacts on coastal rivers.....	10
CHAPTER 3: METHODOLOGY	14
3.1. Numerical modeling.....	14
3.2. Distribution analysis and eigen-analysis.....	23
3.3. Sea-level rise projection.....	25
CHAPTER 4: VALIDATION	27
4.1. Time-series analysis	27
4.2. Distribution analysis and eigen-analysis.....	34
4.3. Model sensitivity with regard to salinity-field initial condition.....	38
CHAPTER 5: ANALYSIS	41
5.1. Sea-level rise impacts.....	41
5.2. Implications on estuarine biology	51
CHAPTER 6: CONCLUSIONS	56
LIST OF REFERENCES	60
VITA	67

LIST OF TABLES

Table 1: Details of the ten runs that were completed in this study.	27
Table 2: Errors (see Equations 7-9) computed from the model-data fits for Runs 1 and 2 and from the eigen-analysis-model fits based on accumulation of the first ten principal components (PCs). Units of RMSE are ppt. SI and IA are expressed as unitless measures.	30
Table 3: Values of $\ (ds/d\delta)_{\delta=0}\ $, p_4 , p_3 and p_5 for the four salinity-gauging stations and 13 pre- identified tributaries. See Equations (13) and (14) for reference.	45

LIST OF FIGURES

Figure 1: A total of 13 tributaries of the lower St. Johns River and four interior stations are used to validate the model.	2
Figure 2: The model bathymetry, finite element mesh and initial conditions of salinity for the lower St. Johns River are shown side-by-side.	18
Figure 3: Boundary conditions for the numerical modeling.	20
Figure 4: Time-series salinity records of data and model results at Dames Point (river km 20) for the 10-year record (1997–2007).	30
Figure 5: Time-series salinity records of data and model results at Acosta Bridge (river km 40) for the 10-year record (1997–2007).	31
Figure 6: Time-series salinity records of data and model results at Buckman Bridge (river km 60) for the 10-year record (1997–2007).	32
Figure 7: Time-series salinity records of data and model results at Shands Bridge (river km 80) for the 10-year record (1997–2007).	33
Figure 8: CDFs of salinity (data and model: present-day conditions—Run 2 and sea-level rise of 0.30 m—Run 10) for the four salinity-gauging stations located in the lower St. Johns River.	35
Figure 9: The eigen-analysis results include PC values for the first two PCs over the 200-km length of the lower St. Johns River and reconstituted salinity records generated from PC1 and PC2.	36
Figure 10: Salinity ratios ($S_{Runn}:S_{Run2}$) based on Runs 2–6 for the four salinity-gauging stations located in the lower St. Johns River.	39

Figure 11: Linear and nonlinear change in salinity due to sea-level rise for the four salinity-gauging stations located in the lower St. Johns River.	45
Figure 12: Plots for the 200-km length of the lower St. Johns River, including values of: a) p_4 ; b) $p_4:p_5$; c) p_3 ; and d) Δq_{cum} . The vertical dashed lines are for reference as related to the discussion in the text.....	48
Figure 13: A total of 81 species are defined in terms of salinity tolerance, including average and standard deviation.	51
Figure 14: Salinity tolerance, location in the river for present-day conditions and migration (change in river location) due to sea-level rise / increasing salinity for the 81 species.....	52

ABSTRACT

The lower St Johns River is a low-gradient coastal river with tidal hydrodynamics that remain active from the Atlantic Ocean through to the upstream end of Lake George (river km 200). Salinity in the lower St Johns River is spatially and temporally variable, whereby the salinity distribution is driven primarily by the combination of ocean processes of tides and storm surges and hydrological processes of watershed runoff. This study examines the probability distributions and modes of behavior of salinity for present-day conditions using data, numerical modeling and eigen-analysis. The hypothesis is that long-term changes (decadal scale) in the ocean processes will cause the probability distributions of salinity to adjust, and therefore there is a quantifiable non-stationarity of salinity in the lower St Johns River (shifts in the probability distribution of salinity, as representative of salinity increase) due to sea-level rise. The numerical modeling is validated against data, then the model is applied to generate synthetic salinity records for the main river stem and tributaries of the lower St. Johns based on present-day conditions. The synthetic salinity records are transformed into probability distribution functions (PDFs) and eigen-functions. The same analysis is performed on synthetic salinity records generated by the model when applied in forecast mode (i.e., sea-level rise). Comparisons of the forecasted PDFs and eigen-functions with those for present-day conditions quantify the non-stationarity (shifts in probability distributions and changes in eigen-structure) of the salinity in the lower St Johns River. The underlying physics of the cause (sea-level rise)-effect (non-stationarity of salinity) relationship are assessed in terms of coastal/river hydrodynamics.

CHAPTER 1: INTRODUCTION

The lower St. Johns River is a macrotidal estuary located in northeast Florida (see Figure 1) with tidal hydrodynamics that persist through the extent of Lake George (river km 200). The impact of sea-level rise on the salinity in estuaries is an issue that hasn't received adequate attention, especially given the amount of work that's been done towards the study of the impact of sea-level rise on hydrodynamics in these very same estuaries. There is justified reasoning that sea-level rise will cause the salinity in estuaries to increase as a result of the associated (elevated) offshore water level. Estuaries are continuously fluctuating geologically (sedimentation and erosion), hydrodynamically (tides and storm surge) and environmentally (salinity and biota) as they tend toward a new equilibrium with the surrounding boundary conditions; e.g. ocean sea level. Therefore, a relationship exists between sea-level rise and the stationarity/non-stationarity of salinity behavior, i.e., either a fixed or moving frequency distribution of salinity results from an estuary subject to sea-level rise. This study investigates potential sea-level rise impacts on salinity (and the associated spatial variability of non-stationarity) in the lower St. Johns River.

The thesis is organized as follows. Chapter 2 is a literature review that provides background and context on existing conditions of the lower St. Johns River and sea-level rise impacts on estuaries, in general. Chapter 3 contains the methods used in the thesis, including the

numerical modeling and eigen-analysis. The validation of the methods used in the thesis are contained in Chapters 4, followed by the discussion in Chapter 5. Chapter 6 concludes the thesis.

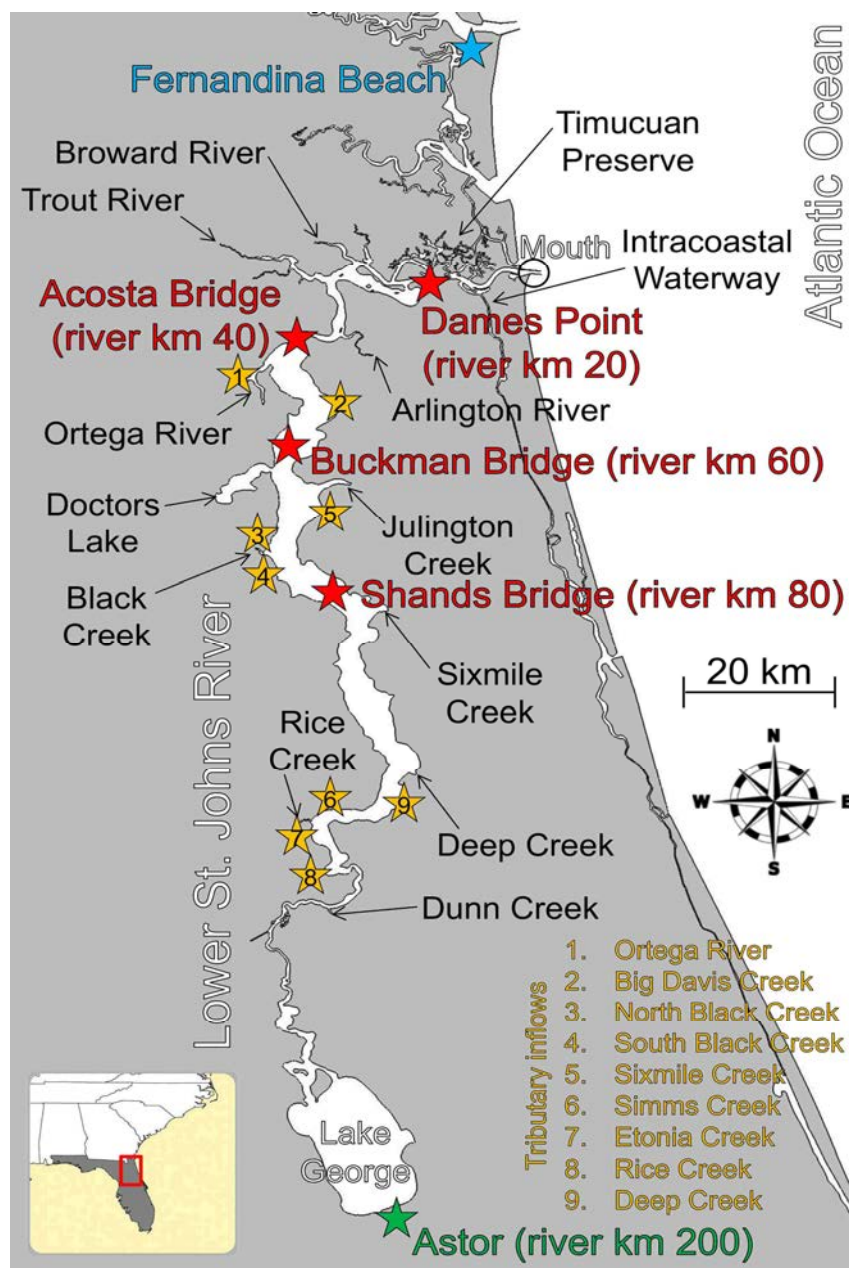


Figure 1. Map of the St. Johns River

CHAPTER 2: LITERATURE REVIEW

The following literature review aims to highlight two main topics directly related to the present study. Firstly, the existing knowledge of the lower St. Johns River is presented to provide an understanding of the importance of the river to the northeast Florida region. Existing knowledge of salinity is a focal point of this first segment of the literature review. Secondly, previous studies involving the impacts of sea-level rise on coastal rivers are documented to highlight past advancements and demonstrate the need for more studies concerning this specific issue. Background of the physics associated with salinity trends is given to provide context for interpretation of the results from the present study.

2.1. Existing knowledge of the lower St. Johns River

The lower St. Johns River is of historic (and other) importance to northeast Florida, and it has, and continues to be, studied heavily over a wide range of subjects. In this section, previous studies of hydrodynamics and salinity in the lower St. Johns River are presented as related to: the theory/concept of the lower St Johns River as a macro-tidal riverine estuary; data, monitoring and observation; and modeling (numerical and eigen-analysis).

2.1.1. Theory/concept of the lower St. Johns River as a macrotidal riverine estuary

The lower St. Johns River is located in northeastern Florida, which starts at the Ocklawaha River in Putnam County, Palatka, and flows downstream (northward) into the Atlantic Ocean in Duval County, Jacksonville (Toth, 1993). According to Morris (1995) the St. Johns River is the longest north-flowing river in the United States (over 300 miles) and the longest river in Florida. The landscape features of the river, including the watershed basin, are large and flat with direct contribution of freshwater runoff into the river (Bergman, 1992). The St. Johns River is an elongated, shallow estuary with a sizeable floodplain. According to Toth (1993) the St. Johns River is elevated above sea-level near the headwaters of the river, with an average gradient of the main river channel of only 0.022 m/km (0.1 ft/mile), which strengthens the argument of the flat nature of the river. Owing to the low gradient of the river, the St. Johns River is tidal throughout its total length of over 500 km (310 mile) (Livingston, 1991). Thus, tidal activity will affect the entire lower St. Johns River as well as the lower reaches of its tributaries. The average tidal amplitude is 1.5 m (4.9 ft) at the ocean inlet and changes unevenly upstream as a result of channel morphology (Toth, 1993). The lower St. Johns River is fed by 12 major tributaries, each named after the major tributaries flowing through them. A thirteenth basin represents the minor tributaries draining directly into the St. Johns River (Bergman, 1992). Bergman (1992) continues to state that most precipitation in the lower St. Johns River occurs during the summer from June through to September. Within this period, rainfall is driven primarily by convectional activity and tropical cyclones, and averages around 0.66 m (26 in), and accounts for almost half of the average yearly basin rainfall. In the winter, however, rainfall is generally driven by frontal activity owing to large scale weather developments. Thus, winter rainfalls tend to last for days and are known to affect larger areas than typical summer showers. The average yearly basin rainfall for December through

to March is about 0.32 m (12.5 in). It is important to grasp the hydrological aspects of the lower St. Johns River as they will facilitate in understanding the salinity trends in the river, which is the focus of this paper.

The St. Johns River is also an estuary, where there is an exchange and mixing of saline (ocean) water with watershed-derived freshwater. As the river's current encounters the sea's tide, the saline water from the sea finds its way into the river mouth and thus dilutes the quality of the freshwater. Salinity can be defined as the concentration of salts in a body of water, with ocean salinity having a measure of 35 (or higher) parts per thousand (ppt) and rainwater and tributary discharge usually close to a measure of 0 ppt. Toth (1993) pointed out that the measure of salinity at a given location in the river is the result of mixing between freshwater and saltwater. The chemical composition of the water in the St. Johns River changes from seawater near the mouth to freshwater further upstream, which is indicative of the progressive mixing between the saline and freshwater along the rivers reach (U.S. Geological Survey, 2013). The measure of salinity at Dames Point Bridge (USGS) ranged from approximately 0.3 to 38.7 ppt during 1996-2001 and 2003-2011 (U.S. Geological Survey, 2013). The measure of salinity at Acosta Bridge (USGS) ranged from 0.1 to 34.5 ppt during 1995-2001. In a study conducted by Bacopoulos, Kubatko, Hagen, Cox, & Mulamba (2016), where "continuous data of vertical-profile salinity were analyzed for four stations located successively upriver in a macrotidal estuary, the lower St. Johns River", it was concluded that the river displayed characteristics of a well-mixed estuary. The most vertical variability of salinity, a mere 1.3 ppt, was observed at Dames point (river km 20). An ongoing debate exists as to whether the use of a two-dimensional depth integrated model (2DDI) is plausible for hydrodynamic-salinity modeling of the St. Johns River. Bacopoulos et al. (2016) stand using a 2DDI model for the lower St. Johns River, stating that the "well-mixed salinity

conditions and dominant horizontal structure of salinity variations in the river make it suitable for the use of a barotropic two-dimensional modeling approach for hydrodynamic-salinity transport.”

Salinity in the lower St. Johns is spatially and temporally variable, whereby the salinity is driven primarily by a combination of coastal processes of tides and storm surge and hydrological processes of watershed runoff. This paper, however, seeks to hone in on the coastal processes involved, sea-level rise specifically, in order to analyze and quantify its effects on the salinity in the lower St. Johns River.

2.1.2. Data, monitoring and observation

There is an immense amount of hydrodynamic and salinity data for the lower St. Johns River, and the purpose of this section is to identify some of the more prevalent data sources while also consolidating these sources into an organized review. Some of the agencies that provide/avail data include: NOAA (National Oceanographic and Atmospheric Administration)/ NOS (National Ocean Service), USGS (United States Geological Survey), SJRWMD (St. Johns River Water Management District) and SJR Report (St. Johns River Report). Collectively these agencies provide a wide range of data including: water level and current data, salinity data, discharge and streamflow data, as well as information concerning the biology in the St. Johns River.

NOAA’s Center for Operational Oceanographic Products and Services website (CO-OPS) makes tide and current data readily available to the public. According to NOAA NOS (2016), CO-OPS is one of the most trusted sources for accurate, dependable, and up-to-date water-level and current measurements. Concerning the water level data, which is an essential part of this paper, CO-OPS provides a wide range of rich information relating to real-time water level data, predicted

tide data and tidal datums. With regard to current data, the agency provides tidal current predictions as well as real-time and historic current data, although these data are far more scarce than water level data.

Likewise, USGS provides the public with a vast amount of useful data. By way of Water Quality Watch, USGS provides continuous real-time water quality information. The water quality data include, but are not limited to: temperature, pH, turbidity, and specific conductance (salinity). U.S. Geological Survey (2016a) states that these data are made available at more than 1300 stations across the US. USGS also provides real-time streamflow/discharge data at many locations throughout the US, over 4200 stations according to (U.S. Geological Survey, 2016a). The streamflow/discharge data at these stations are recorded in 15- to 60-minute increments, whereas the water quality measurements discussed earlier are recorded in 5-minute to hourly intervals. Both the salinity and streamflow/discharge data made available by USGS played an important role in this paper.

For many years, the SJRWMD and SJR Report have gathered and processed data concerning the St. Johns River that has proved very informative. The data most relevant to this paper being: rainfall, surface water levels and water quality data. SJRWMD (2016) provides data for a number of stations that observe characteristics such as river discharge, rainfall, surface and groundwater quality conditions. Both short- and long-term trends of these characteristics in the water are monitored and utilized in predicting future conditions of the water in the St. Johns River.

2.1.3. Numerical modeling and eigen-analysis

The two numerical models covered in this sub-section are trusted and regarded favorably within the coastal and river modeling community for salinity simulation, and have been heavily scrutinized to ensure they continue to develop and produce accurate and dependable results. The models are known by the acronyms ADCIRC (Advanced Circulation) and EFDC (Environmental Fluid Dynamics Code). The former is used widely in academia and private practice, whereas the latter is more prevalently used in public agencies and private industry (JU/UNF, 2016). The ADCIRC code (Luettich Jr., Westerink, & Scheffner, 1992) is a two-dimensional hydrodynamic model that is able to simulate water levels and depth-integrated velocities for tide, wind and freshwater river influx forcing. Continued work from Kubatko, Westerink, & Dawson (2006) on the ADCIRC code produced what is known as DG-SWEM. DG-SWEM is essentially ADCIRC with salinity transport on top of the hydrodynamics. The DG in DG-SWEM also differentiates it from ADCIRC in that DG-SWEM uses a discontinuous-Galerkin finite element method. DG-SWEM, which will be discussed in greater detail later, was purposefully designed within the ADCIRC framework so as to keep all other file types and code settings intact. The salinity modeling capabilities of ADCIRC which make it attractive for public/private use include advection-diffusion, surface wind stress, unstructured triangulation and two-dimensional flows. EFDC is a three-dimensional hydrodynamic and transport model that can simulate changes in velocity, discharge, water levels and salinity. The features that make EFDC attractive for salinity modeling in the lower St. Johns River include advection-diffusion, surface wind stress, two- and three-dimensional flows and dynamic coupling of salinity and density. JU/UNF (2016) states that “In a qualitative sense, the EFDC model can describe depth-variable flow and salinity, but to

accomplish this, the horizontal resolution is constrained, whereas the ADCIRC model can flexibly resolve the horizontal features of the geometry and physics, but it solves two-dimensional equations and thusly cannot simulate depth-variable physics.” However, Bacopoulos et al. (2016) concluded that the St. Johns River displayed characteristics of a well-mixed estuary, where the depth-dependence of salinity (i.e., stratification) is negligible (JU/UNF, 2016). Given its flexibility in providing horizontal resolution, the ADCIRC model is therefore preferred over EFDC for this thesis.

Eigen-analysis/Empirical Orthogonal Function analysis (Monahan, Fyfe, Ambaum, Stephenson, & North, 2009) is a method employed to observe different modes of behavior (patterns) of variability and how they change over time. Most often, the EOFs are found by computing the eigen-values and eigen-vectors of a covariance matrix. The computed eigen-values give a measure of the percent variance described by each mode. An example of this is evident in a study done by Henrie & Valle-Levinson (2014) on subtidal variability in water levels inside a subtropical estuary. Therein, it’s stated that 96% of the subtidal variability in the lower St. Johns River can be explained by the first EOF alone. While eigen-analysis has proved effective in providing a better understanding on patterns of variability, literature concerning studies done in the lower St. Johns River where it’s been used is scarce. This thesis seeks to take advantage of this method of analysis (described in greater detail in forthcoming chapters) while looking at how sea-level rise impacts the salinity in the lower St. Johns River.

2.2. Sea-level rise impacts on coastal rivers

The question as to whether sea level is rising is a controversial topic of today. There are many that argue in favor of the notion that sea level is rising, and within this group there is a question as to the actual magnitude of the positive rate of change. Bilskie, Hagen, Medeiros, & Passeri (2013) concluded that the growing number of people migrating to coastal cities along with factors such as nearshore geomorphology and sea-level rise have a direct impact on how storm surge and the associated inundation behave in coastal communities. As a result of these factors, new areas will become susceptible to coastal flooding and regions that have already become unsustainable will see an increase in both the frequency and magnitude. Agencies such as NOAA have tidal gaging stations throughout northeastern Florida that report values of sea-level rise based on linear regression analysis, allowing for the forecast of sea-level rise as far as 2080 (Walton, 2007).

Sea-level rise is a byproduct of climate change that can have substantial effects on the coastal environment (Hagen & Bacopoulos, 2012). Bilskie et al. (2013) pointed out that low-lying coastal regions are most vulnerable to the impacts of climate change, especially sea-level rise. The short- and long-term effects of sea-level rise on rivers include, but are not limited to changes in tidal hydrodynamics, salt marsh migration and changes in salinity, all of which have consequences for navigation, fisheries, shoreline erosion and coastal flooding (Bilskie et al., 2013; Passeri, Hagen, Medeiros, & Bilskie, 2015). Sea-level rise impacts on hydrodynamics entail a general increase in tide and storm surge levels along the coast and in coastal rivers, which adds to the present-day extent of inundation within the adjacent floodplains. Increasing salinity poses a problem because it may render the quality of the water in the lower reaches of

coastal rivers unsuitable for biology and domestic, agricultural, industrial and other uses, thus damaging the river health and recreational value of areas in the lower portions of a river basin. Salt marshes make up a vast area of most estuarine environments and are one of the most endangered ecosystems when considering sea-level rise (Church & White, 2006). This is owing to the direct impact that sea-level rise has on the biomass density (productivity) of the marshes.

A rising sea level is an indicator of climate change, which can pose a threat to the coastal environment. One such threat presents itself in the form of coastal flooding. The response in coastal flooding due to sea-level rise can be either linear or nonlinear. This was noted in a study by Hagen & Bacopoulos (2012), where they investigated coastal flooding in Florida's Big Bend region with application to sea-level rise based on synthetic storm surge analysis. Therein, the differences between a linear and nonlinear response to coastal flooding were described. A linear response can be equated to a static response, whereby existing dynamics simply shift in elevation by the amount of sea-level rise. However, the nonlinear response is much more dynamic, and acts to adjust the linear response either upwards or downwards in the face of sea-level rise. The dynamic approach takes into account the nonlinear effects that exist in the process. The study concluded that the impact of sea-level rise in Florida's Big Bend Region, for periods of both extreme storm surge and astronomic tides, should be analyzed as a dynamic process rather than a static process, owing to the possibility of missing dynamic interactions when using a static approach. Bacopoulos & Hagen (2014) also considered the impact of sea-level rise on coastal environments through the lens of hydrodynamics. Their study focused on the dynamic considerations of sea-level rise with respect to water levels and flooding in Apalachicola Bay, where once more the question of dynamic approach vs static approach (for water-level boundary conditions and flooding extent analyses) presented itself. The results of the study showed that in

the case of flooding, dynamic vs static is not a one-to-one ratio, but rather that the dynamic approach outweighed the static approach by a factor of $4/3 - 5/3$. In the case of water levels, applying a statically adjusted offshore boundary condition was found to be sufficient due to the linearity of the offshore environment, relative to the nonlinearity of the inshore environment. In a paper by Passeri et al. (2015) on the impacts of historical morphology and sea-level rise on tidal hydrodynamics in a microtidal estuary, it was stated that “sea-level rise has the potential to alter astronomic tidal hydrodynamics by increasing tidal ranges, tidal prisms and inundation as well as changing current velocities and circulation patterns.” Friedrichs, Aubrey, & Speer (1990) went on to say that “within estuaries, tidal asymmetries and resulting sediment transport patterns can be fundamentally altered if rising sea levels increase channel depths.” The results of their study highlighted the importance of taking into account changes in morphology when assessing sea-level rise. Results from a study conducted by French (2008), relating to the Blyth estuary (a mesotidal estuary in eastern England), indicated that a 0.3-m increase in sea level could result in peak tidal current velocities and discharges increasing by values upwards of 20%.

Coastal salt marshes serve as both a habitat for a variety of species (Halpin, 2000; Pennings & Bertness, 2001) and protective mechanism for shorelines. They perform the latter by decreasing the energy of incident waves, and increasing friction, thus dissipating flow energy (Alizad et al., 2016). Sea-level rise affects the normal behavior of salt marshes, and on many occasions existing marshes are unable to accrete quickly enough to protect themselves from increasing sea-level rise (Donnelly & Bertness, 2001; Warren & Niering, 1993), ultimately resulting in complete submergence or loss (Nyman, DeLaune, Roberts, & Patrick Jr, 1993). The same ideas were shared by Bilskie et al. (2013) in stating that, when sea level rises at a pace that is too rapid for sediment accretion to keep up, the salt marshes in a coastal environment tend to

migrate or transform to open water. According to Hagen et al. (2012), in a case where no accretion of sediment occurs, there would be a drop in the net production of marsh vegetation throughout the whole marsh landscape, even if subjected to a moderate increase in sea level . A study by Alizad et al. (2016) used a spatially-explicit model that coupled astronomic tides and *Spartina alterniflora* dynamics to investigate how sea-level rise influenced salt marsh productivity in northeast Florida. It was concluded therein that “marsh productivity is primarily a function of relative elevation, MHW and accretion relative to sea-level rise.” Sea-level rise perturbs existing tidal levels, particularly MHW, thus affecting the productivity of the salt marshes.

Sea-level rise has been documented as a known threat to coastal environments around the world for various reasons. However, very little attention has been given to the issue of sea-level rise impacts on salinity. The study of salinity in the lower St. Johns River is relatively scarce, compared with the large knowledge base covering its hydrodynamics, and is limited to Sucsy & Morris (2002) and Bacopoulos et al. (2016). Furthermore, there is limited investigation of salinity trends in estuaries (e.g., Wiseman, Swenson, & Power, (1990) studied Louisiana estuaries and Shellenbarger & Schoellhamer, (2011) studied San Francisco estuary). This thesis strives to add to the body of knowledge dealing with salinity in the lower St. Johns River, as well as how salinity will change due to sea-level rise. Given what was learned from previous studies dealing with sea-level rise impact analysis, herein a dynamic approach is applied so as to be able to examine any nonlinearity vs linearity of sea-level rise impacts on salinity.

CHAPTER 3: METHODOLOGY

3.1. Numerical modeling

3.1.1. Numerical modeling approach

DG-SWEM (discontinuous-Galerkin, shallow-water equations model) is a two-dimensional, depth-integrated finite element model used to simulate tidal hydrodynamics and salinity transport (Kubatko et al., 2006). DG-SWEM solves the vertically integrated equations of mass and momentum conservation, based on the hydrostatic pressure approximation, and the advection-diffusion equation for salinity transport. Models based on the DG-SWEM code have been used extensively to simulate long wave processes such as astronomical tides and hurricane storm surges (Bacopoulos & Hagen, 2009; Bunya et al., 2010). Specific to this thesis, a Manning's friction formulation is used, baroclinic terms are neglected and the advection terms are employed, resulting in the following set of equations, presented in a cartesian coordinate system (Kolar, Westerink, Gray, & Jr., 1994):

$$\frac{\partial \zeta}{\partial t} + \frac{1}{R \cos \phi} \left[\frac{\partial UH}{\partial \lambda} + \frac{\partial (VH \cos \phi)}{\partial \phi} \right] = 0 \quad (1)$$

$$\frac{\partial U}{\partial t} + \frac{1}{R \cos \phi} U \frac{\partial U}{\partial \lambda} + \frac{1}{R} V \frac{\partial U}{\partial \phi} - \left(\frac{\tan \phi}{R} U + f \right) V \quad (2)$$

$$= - \frac{1}{R \cos \phi} \frac{\partial}{\partial \lambda} \left[\frac{P_s}{\rho_0} + g(\zeta - \alpha \eta) \right] + \frac{1}{H} M_\lambda + \frac{\tau_{s\lambda}}{\rho_0 H} - \tau_* U$$

$$\frac{\partial V}{\partial t} + \frac{1}{R \cos \phi} U \frac{\partial V}{\partial \lambda} + \frac{1}{R} V \frac{\partial V}{\partial \phi} + \left(\frac{\tan \phi}{R} U + f \right) U \quad (3)$$

$$= - \frac{1}{R} \frac{\partial}{\partial \phi} \left[\frac{P_s}{\rho_0} + g(\zeta - \alpha \eta) \right] + \frac{1}{H} M_\lambda + \frac{\tau_{s\phi}}{\rho_0 H} - \tau_* V$$

where depth-integrated momentum dispersion in the longitudinal and latitudinal, respectively, is given by

$$M_{\lambda, \phi} = \frac{E_{h/2}}{R^2} \left[\frac{1}{\cos^2 \phi} \frac{\partial^2 (U, V) H}{\partial \lambda^2} + \frac{\partial^2 (U, V) H}{\partial \phi^2} \right] \quad (4)$$

and bottom friction in the longitudinal and latitudinal directions, respectively, is given by

$$\tau_* = \rho(U, V) C_f \sqrt{U^2 + V^2} \quad \text{and} \quad C_f = \frac{g}{H^{1/3}} n^2 \quad (5)$$

where τ_* represents stress due to bottom friction, ρ is the density of seawater, C_f is the bottom coefficient, H is the height of the local water column, g is gravity and n is the Manning's n coefficient, which is measured in units of $\text{m}/\text{s}^{1/3}$. For the equations (1) - (3) listed above, t = time; λ , ϕ = degrees longitude (east of Greenwich positive) and latitude (north of the equator positive), respectively; U, V = depth-integrated velocity in the longitudinal and latitudinal

directions, respectively; H = total height of the water column, $h + \zeta$; h = bathymetric depth, relative to MSL; ζ = free surface elevation, relative to MSL; R = radius of the Earth; $f = 2\Omega \sin \phi$ = Coriolis parameter; Ω = angular speed of the Earth; P_s = atmospheric pressure at the free surface; ρ_0 = reference density of water; g = acceleration due to gravity; α = Earth elasticity factor; $E_{h/2}$ = horizontal eddy viscosity; $\tau_{s\lambda}$, $\tau_{s\phi}$ = applied free surface stress in the longitudinal and latitudinal directions, respectively; τ_* = quadratic bottom stress; and η = Newtonian tide potential (Reid, 1990).

The advection-diffusion equation is solved in its conservative form, which compactly can be presented as:

$$\frac{\partial C}{\partial t} + \mathbf{v} \cdot (\nabla C) - \nabla \cdot (D \nabla C) = 0 \quad (6)$$

where C is the concentration of salinity, \mathbf{v} is the advective velocity and D is diffusivity. The mathematical operators in the advection-diffusion equation are gradient (∇) and divergence ($\nabla \cdot$)

Pertaining to DG-SWEM for this study, numerical flux was solved using a local-Lax Friedrichs method and piecewise polynomial functions (functions that are characterized by polynomial sub-domains) were used in space (Kubatko, Bunya, Dawson, Westerink, & Mirabito, 2009). A Runge–Kutta time stepping scheme (Kubatko, Dawson, & Westerink, 2008) ,i.e., a two stage, second-order scheme, was applied in this thesis.

It may also be relevant to point out that the approximation of the lower St. Johns River in this model is absent of significant regions of wetting and drying. The computational mesh is intended to describe hydrodynamics within the boundaries of the river banks, where wetting and drying has almost no effect on the simulations (e.g., see Bacopoulos et al. 2009). The finite

element mesh has been inspected and deemed accurate for hydrodynamic (Bacopoulos, Hagen, Cox, Dally, & Bratos, 2012) and salinity (Bacopoulos et al., 2016) simulation in the lower St. Johns River (Figure 2). The mesh resolves the entire 200-river-km stem of the lower St. Johns River as well as its many tributaries with resolution of 25–250 m.

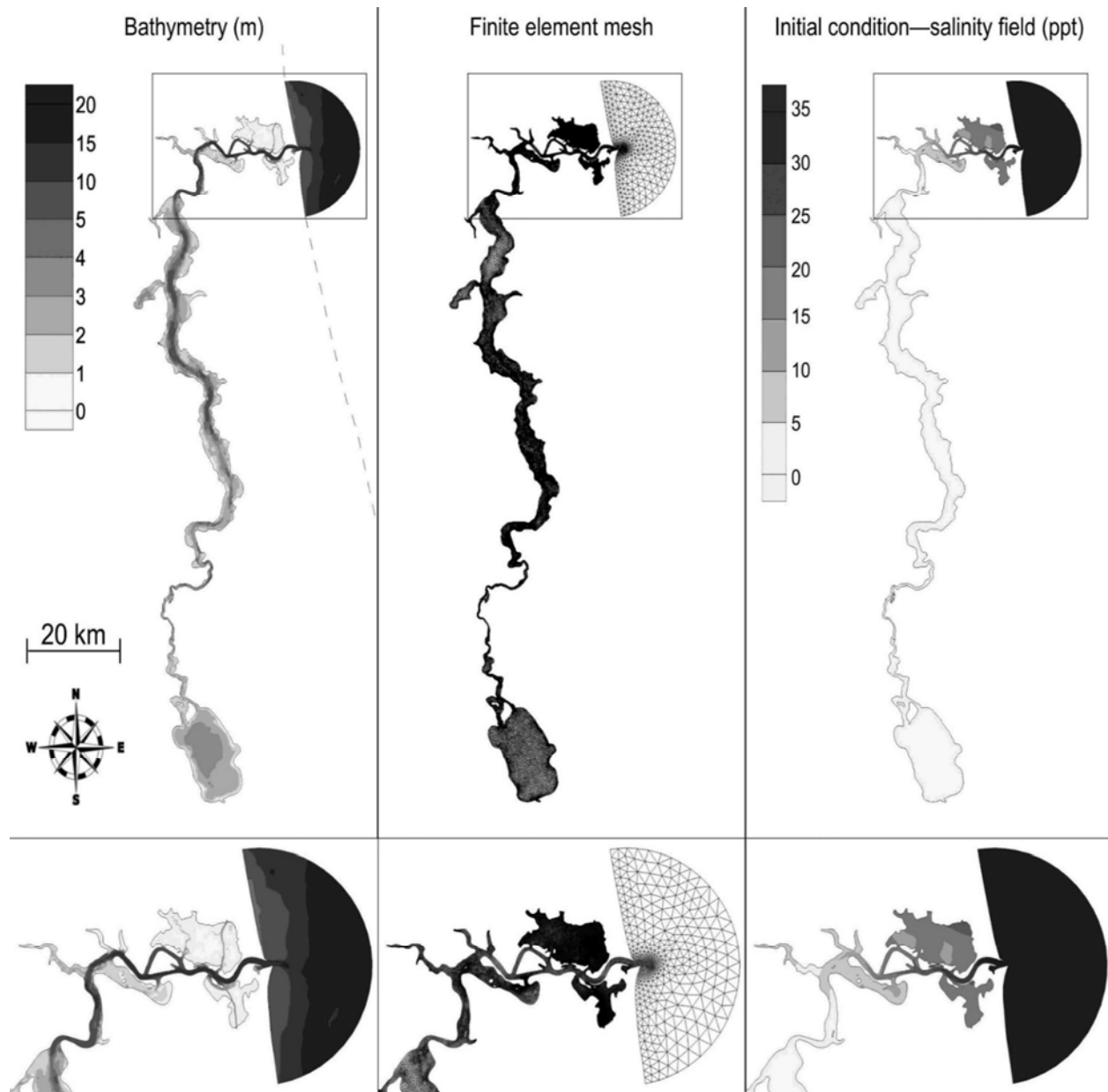


Figure 2. The model bathymetry, finite element mesh and initial conditions of salinity for the lower St. Johns River are shown side-by-side. Initial conditions of salinity were built using data available from four interior salinity-gauging stations (river km's 20, 40, 60 and 80) and assumptions of saline water (35 ppt) for the offshore boundary and freshwater (0.2 ppt) for the upstream boundary. Four error-induced hypothetical cases (not shown) employ $\pm 5\%$ and $\pm 10\%$ station-wide adjustment of the data-based initial condition.

The modeling approach used in this study with DG-SWEM is rather simple in its design. The model is forced at the upstream boundary (river km 200) and river-tributary boundaries (total of 9) with hydrologic-inflow data. The model is also forced at the downstream boundary (offshore) with sea-level data. Figure 1 shows the locations of the data sites used for constructing the model forcing (i.e., boundary conditions). Boundary conditions for DG-SWEM were obtained from continuous water-level data for the offshore boundary (Fernandina Beach—8720030; (NOAA NOS, 2016)) and continuous freshwater-inflow data for the upstream boundary (Astor—02236125; (U.S. Geological Survey, 2016b)) and river-tributary boundaries (Figure 1 contains the nine stations). Fernandina Beach is located approximately 25 km north of the St. Johns River mouth. Astor is located approximately 200 km upstream the lower St. Johns River, at the entrance to Lake George. The nine tributary-inflows are located along the length of the lower St. Johns River, as seen in Figure 1.

The data used to formulate the boundary conditions are shown in Figure 3. NOAA reports water-level data in two formats: verified data, which are actual measurements of water level, but are not always available due to instrument, communication and/or other fatal error; and predicted tides, which are estimates of the water level based on tidal resynthesis, which provides a continuous (gapless) signal. The water-level record contains a total of 87,648 data points, where 96% of the record is composed of verified data. Predicted tides were used to fill in the gaps of the record (4% in total) when verified data were not available. A residual signal was calculated as the verified data (when available) minus the predicted tides to provide a non-tidal measure of the offshore boundary condition.

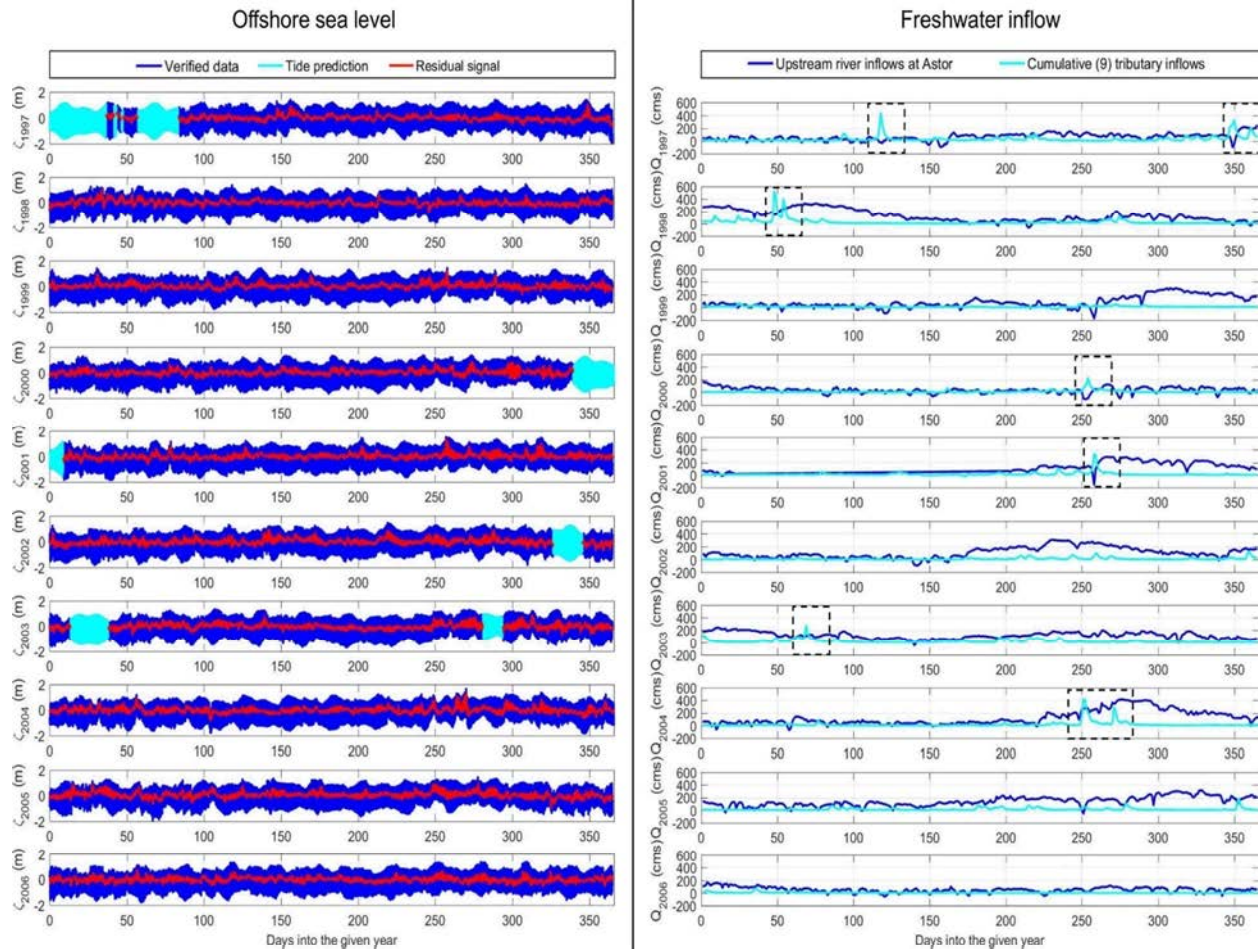


Figure 3. Boundary conditions for the numerical modeling involve data for offshore sea level (Fernandina Beach) and freshwater inflows, including upstream-river discharge (Astor) and local-watershed discharge (nine tributaries), over the 10-year record (1997–2007). The offshore sea level data are shown as the actual water level measured (verified data), reconstituted astronomic tide signal (predicted tide) and non-tidal water level (residual). The local-watershed discharge data are shown as the cumulative inflow for the nine tributaries. The dashed-line boxes denote some of the major events apparent in the inflow records.

The freshwater-inflow data are gapless for the full ten years with the exception of January 22 – July 20, 2001. Linear interpolation was used to fill the data gap of the inflow record.

Negative inflow means reverse (upstream) flow, which occurs sporadically over the record.

There are events in the inflow records that depict relatively quick flashes of tributary inflow that occur simultaneously with negative inflow or reduced flows for the upstream river inflow, each of which is followed by a (sometimes prolonged) period of (sometimes high) discharge (e.g., see annotations in Figure 3). The events cause a quick pulse of flood in the river, as a result of coastal storm surge, which is responsible for the short-lived upstream flow reversals, while the tributaries respond near immediately with a burst of discharge, owing to local watershed rainfall-runoff. The duration of upstream river discharge following each of the events is the result of the relatively longer time required for the large-sized upper and middle river basins to generate discharge from the greater watershed rainfall-runoff.

The offshore sea-level data were assembled into a stage boundary condition (fort.19 file type; refer to (ADCIRC, 2016)) and the upstream and tributary hydrologic-inflow data were assembled into a flux boundary condition (fort.20 file type; refer to (ADCIRC, 2016)). The stage boundary condition was resolved at hourly increment and the flux boundary condition was resolved at daily increment, and both boundary conditions covered the entire 10-year record (1997–2007). The raw offshore sea-level data were converted from MSL datum to NAVD88 datum, so that the stage boundary condition would be consistent with the mesh bathymetry and model calculations (i.e., NAVD88). The raw hydrologic-inflow data were converted from $\text{ft}^3 \text{s}^{-1}$ to $\text{m}^3 \text{s}^{-1}$, so that the flux boundary condition would be consistent with the model calculations (i.e., International System of Units—meters).

An in-depth look at how to set up the model can be found in (Bacopoulos et al., 2016); however, the following is a simple summary of the model parameters and settings: nonlinear (quadratic) bottom friction with Manning's roughness formulation (uniform $n = 0.025$); nonlinear advection; nonlinear finite amplitude effects; horizontal eddy viscosity of $0 \text{ m}^2 \text{ s}^{-1}$; spatially variable Coriolis parameter; and time step of 1.5 s. The model was initialized from a cold start (i.e., still-water condition) with a spin-up of the boundary forcing over the first three days of the simulation. The model was run for a total of 3656 days, which ranges from December 28, 1996 – January 1, 2007. The model runs were contiguous, i.e., the model was not restarted for any reason once it was up and running.

To get a better sense of the sensitivity of the model to initial conditions of salinity, the time required for dynamic equilibrium to be achieved when using a data-based, salinity-field initial condition and four error-induced hypothetical cases ($\pm 5\%$ and $\pm 10\%$ station-wide adjustment) for model initialization was examined. Data for four interior salinity-gauging stations, including Dames Point (river km 20), Acosta Bridge (river km 40), Buckman Bridge (river km 60) and Shands Bridge (river km 80), as displayed in Figure 1, were used to guide the construction of the data-based, salinity-field initial condition. Two additional points of information that guided the formulation of the initial condition included the assumptions of saline water (35 ppt) for the offshore boundary and freshwater (0.2 ppt) for the upstream boundary. Figure 2 shows a contour map of the data-based initial condition of the salinity field. The hypothetical test cases (not shown) adjusted the data-based initial condition by $\pm 5\%$ and $\pm 10\%$ on a station-wide basis, which were chosen to represent the range of error in the salinity field used as the initial condition.

The error metrics used in later portions of the thesis (for model-vs-data evaluation) were root mean square error (RMSE) (Murphy, 1988):

$$\text{RMSE}(P, O) = \sqrt{\frac{1}{N} \sum_{i=1}^N (P_i - O_i)^2} \quad (7)$$

where RMSE = root mean square error, P = prediction, O = observation and N = total number of error evaluations. The units of RMSE are ppt. A scatter index (SI) was also computed to provide a dimensionless (relative) error measure:

$$\text{SI} = \frac{\text{RMSE}}{\bar{O}} \quad (8)$$

where \bar{O} is the mean value of the observations over the entire data record. The index of agreement (IA) was used as an added non-dimensional error measure of the model-data fit (Wilmott, Robeson, & Matsuura, 2012):

$$\text{IA} = 1 - \frac{\sum_{i=1}^N (P_i - O_i)^2}{\sum_{i=1}^N (|P_i - \bar{O}| + |O_i - \bar{O}|)^2} \quad (9)$$

where IA = 0 indicates complete disagreement and IA = 1 indicates perfect agreement.

3.2. Distribution analysis and eigen-analysis

Histograms were used to represent probability distribution functions (PDFs) of salinity for the 10-year record (1997–2007). Bins of 0.5-ppt increment were specified from 0 to 40 ppt. The data and model results were temporally resolved at an hourly time step; however, if there was no data value for a given time step, then the data and model result for that given time step were excluded from the assembly of the PDF. Cumulative distribution functions (CDFs) were

computed from each PDF by counting the cumulative number of histogram values in all of the bins up to the specified bin. The CDFs are the final results of the distribution analysis, which are used for interpretation of the salinity distributions at different locations, and the nonstationarity that results due to sea-level rise.

Simulation output from DG-SWEM provided the input data for the eigen-analysis. Empirical orthogonal function (EOF) analysis (e.g. Monahan et al., 2009) was applied to time series of salinity for 41 locations along the centerline of the lower St. Johns River. The time series were resolved at hourly increment and span the full ten years of the simulation. The 41 locations are spaced at 5-km interval and range from the river mouth to 200 km upriver (see Figure 1 for reference map). The input matrix (**A**) for the EOF analysis was constructed as time-variability for rows (total of 87,648) and space-variability for columns (total of 41). The input matrix (**A**) was kept as is (not demeaned) for the purpose of including baseline (mean) changes in the eigen-analysis and results. First, the covariance matrix (**C**) was calculated from **A** as:

$$\mathbf{C} = \mathbf{A}\mathbf{A}^T \quad (10)$$

where $[\]^T$ is the transpose operator. Then the normalized eigenvectors (**V**) and eigenvalues (**D**) were computed from **C** using EOF analysis (specifically, MATLAB `eig`). Next, the primary components (PCs) were obtained by projecting the eigenvectors on the input matrix:

$$\mathbf{P} = \mathbf{V}^T \mathbf{A} \quad (11)$$

where **P** contains the PC values. Finally, an estimate of the input matrix (**A_{est}**) was recovered as:

$$\mathbf{A}_{\text{est}} = \mathbf{V}\mathbf{P} \quad (12)$$

where if **A_{est}** = **A**, then the procedure is correct. Herein, the first two PCs, which relate to the first and second eigenvalues, i.e., **D**(1,1) and **D**(2,2), are used to construct **A_{est1}** and **A_{est2}** which are recovered as estimates of the PC components (1 and 2) using the first and second eigenvectors, i.e., **V**(:,1) and **V**(:,2), as input.

3.3. Sea-level rise projection

The projection of sea-level rise is a controversial topic (Baart, von Koningsveld, & Stive, 2012). In this thesis, a sea-level rise of 0.05, 0.15 and 0.30 m were used as representative 50-year projections (i.e., 1997–2007 → 2047–2057), which fall into the range of both moderate (Walton, 2007) and accelerated (Jevreieva, Moore, & Grinsted, 2010; Vermeer & Rahmstorf, 2009) sea-level rise scenarios for the foreseeable future (i.e, next ten years). Sea-level rise was applied as a constant “delta” adjustment to the offshore water level record (1997–2007) used in the boundary condition (i.e., fort.19; refer to (ADCIRC, 2016)). A 50-year projection was selected so that the results are relatable to realistic project lengths dealing with mitigation or other corrective measures, and the planning thereof.

3.4. Model runs

A total of ten runs were completed for this thesis (Table 1). The “constants” of the runs are the finite element mesh, model parameterization and settings, offshore water level and upstream river inflow boundary conditions. The “variables” of the runs are: tributary inflows; initial conditions of salinity field; and sea-level rise. Run 1 is the only simulation to exclude tributary inflows, while all other simulations include tributary inflows. Run 2 is the baseline. Runs 3–6 adjust the data-based, salinity-field initial condition by $\pm 5\%$ and $\pm 10\%$ on a station-wide basis. Run 7 applies a negative (time-backward) sea-level rise of -0.05 m. Runs 8–10 apply positive (time-forward) sea-level rise of $+0.05$, $+0.15$ and $+0.30$ m.

Table 1

Details of the ten runs that were completed in this study.

Run	Tributary inflows	Initial condition	Sea-level rise
1	No	Data-based	—
2	Yes	Data-based	—
3	Yes	−10%	—
4	Yes	−5%	—
5	Yes	+5%	—
6	Yes	+10%	—
7	Yes	Data-based	−0.05 m
8	Yes	Data-based	+0.05 m
9	Yes	Data-based	+0.15 m
10	Yes	Data-based	+0.30 m

CHAPTER 4: VALIDATION

The validation of synthetic salinity records at site-specific locations (river km's 20, 40, 60 and 80) was completed using salinity data gathered at four salinity-gauging stations (see Figure 1 for locations). The data are at an hourly interval and range from as early as January 1, 1997 to as late as January 1, 2007. The longest data record is for Dames Point (3652 days), followed by Buckman Bridge (2464 days), Acosta Bridge (2462 days) and Shands Bridge (1718 days). There are some gaps in the data records. The fullest data record is for Shands Bridge (80% data—20% gap), followed by Acosta Bridge (78%), Dames Point (70%) and Buckman Bridge (70%). Simulation output from DG-SWEM included time-series salinity at the four salinity-gauging stations, resolved at an hourly increment, which allowed for hour-by-hour comparison of the model results against the data. Runs 1 and 2 were the two model runs (Table 1) applicable to the validation.

4.1. Time-series analysis

Figures 4 - 7 show the model-versus-data comparisons of the time-series of salinity at Dames Point, Acosta Bridge, Buckman Bridge and Shands Bridge, respectively. Firstly, the spatial feature of salinity in the river is highlighted by the longitudinal variation of salinity

among the four stations (ranging from river km 20 to river km 80). Salinity at Dames Point is in the higher end of the salinity range (typically in the range of 20–40 ppt) and strongly tidally influenced (the range of fluctuations is on the order of 10 ppt). Salinity at Acosta Bridge is in the middle of the salinity range (typically in the range of 10–30 ppt) and moderately tidally influenced (the range of fluctuations is about 5 ppt). Salinity at Buckman Bridge and Shands Bridge is in the lower end of the salinity range (typically in the range of 0–10 ppt) and mildly tidally influenced (the range of fluctuations is 1–2 ppt). Secondly, salinity at all four stations display sensitivity to non-tidal activity (offshore water level and freshwater inflow), which is most evident in the late-summer events (days 250–300). Events typically involve a drawdown (at times rapid, occurring within 1–2 days) of salinity owing to high freshwater inflow followed by a more gradual (on the order of a week) return to the prior salinity level (e.g. see years 1998-2001). Unfortunately, the model simulation only partially captures the more significant events, as though there is a physical forcing (not in the model) resulting in the fast fall and slow rebound of salinity during the more significant events. Nonetheless, the model simulation performed with RMSE in the range of 1.49–5.34 ppt, SI in the range of 0.23–1.55 and IA in the range of 0.34–0.83 (Table 2). Thirdly, the inclusion of the freshwater inflows (Run 2) for the nine tributary-discharge locations improved the simulation at all four stations, but only by slight measure, e.g. the reduction in SI was at most 0.04 and increase in IA was at most 0.01

Table 2

Errors (see Equations 7-9) computed from the model-data fits for Runs 1 and 2 and from the eigen-analysis-model fits based on accumulation of the first ten principal components (PCs).

Units of RMSE are ppt. SI and IA are expressed as unitless measures.

	Dames Point			Acosta Bridge			Buckman Bridge			Shands Bridge		
	RMSE	SI	IA	RMSE	SI	IA	RMSE	SI	IA	RMSE	SI	IA
Run 1	5.63	0.24	0.78	5.11	0.67	0.83	3.29	1.05	0.68	1.53	1.59	0.33
Run 2	5.34	0.23	0.79	5.01	0.65	0.83	3.22	1.03	0.68	1.49	1.55	0.34
PC1	2.02	0.11	0.81	4.10	0.59	0.34	0.64	0.70	0.19	0.09	0.21	0.12
PC2	1.28	0.07	0.93	1.52	0.22	0.91	0.51	0.56	0.48	0.06	0.15	0.23
PC3	1.26	0.07	0.93	1.40	0.20	0.92	0.43	0.46	0.64	0.06	0.13	0.30
PC4	1.24	0.07	0.93	1.37	0.20	0.93	0.42	0.46	0.65	0.06	0.13	0.30
PC5	1.23	0.07	0.93	1.16	0.17	0.95	0.35	0.38	0.76	0.06	0.13	0.46
PC6	0.93	0.05	0.96	1.12	0.16	0.95	0.33	0.36	0.78	0.06	0.13	0.53
PC7	0.93	0.05	0.96	1.09	0.16	0.95	0.33	0.36	0.78	0.06	0.13	0.54
PC8	0.87	0.05	0.97	0.30	0.04	0.99	0.32	0.35	0.80	0.06	0.13	0.64
PC9	0.76	0.04	0.97	0.25	0.04	0.99	0.32	0.35	0.80	0.06	0.13	0.72
PC10	0.25	0.01	0.99	0.25	0.04	0.99	0.32	0.35	0.80	0.06	0.13	0.77

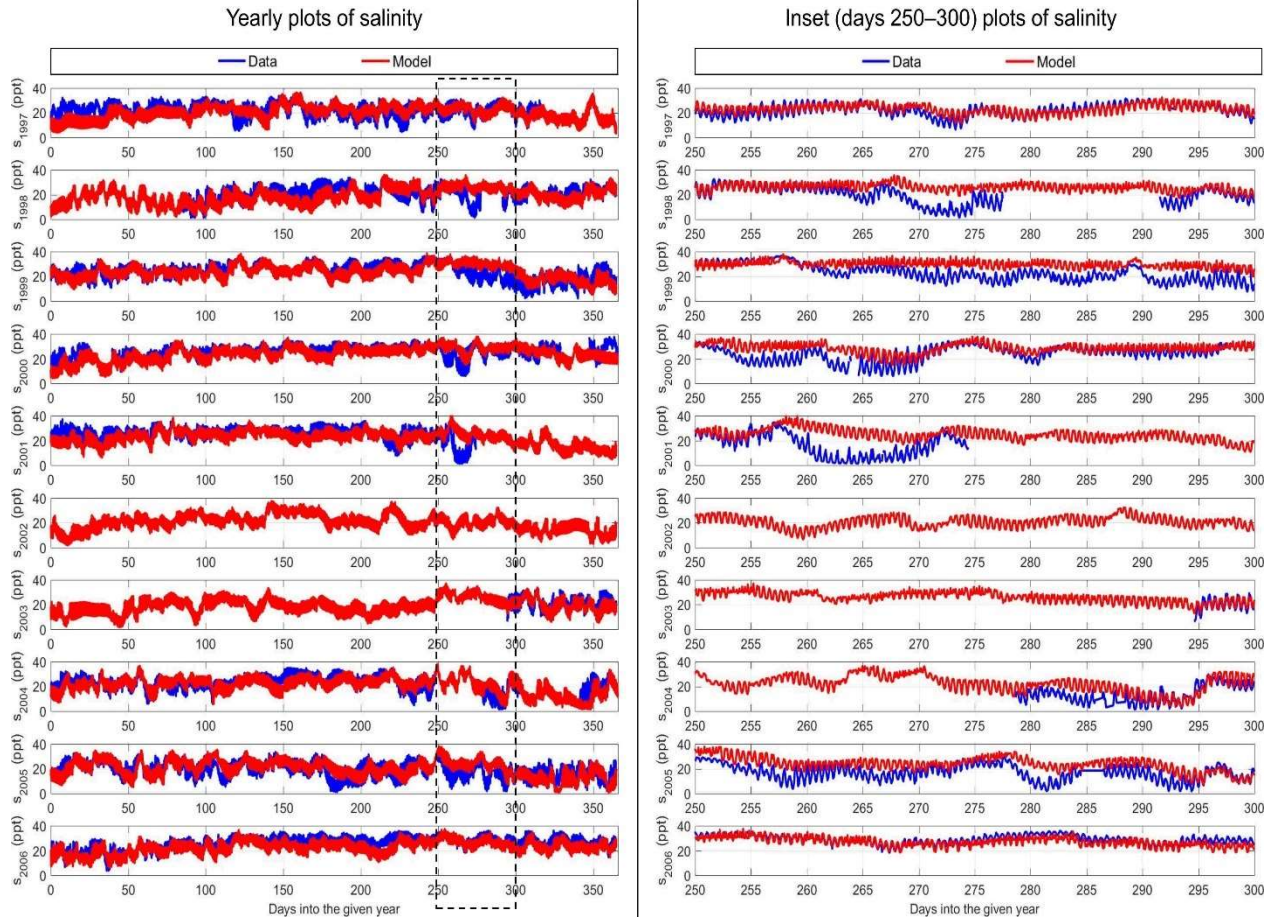


Figure 4. Time-series salinity records of data and model results at Dames Point (river km 20) for the 10-year record (1997–2007). The model results shown are from simulations with tributary inflows included in the model runs.

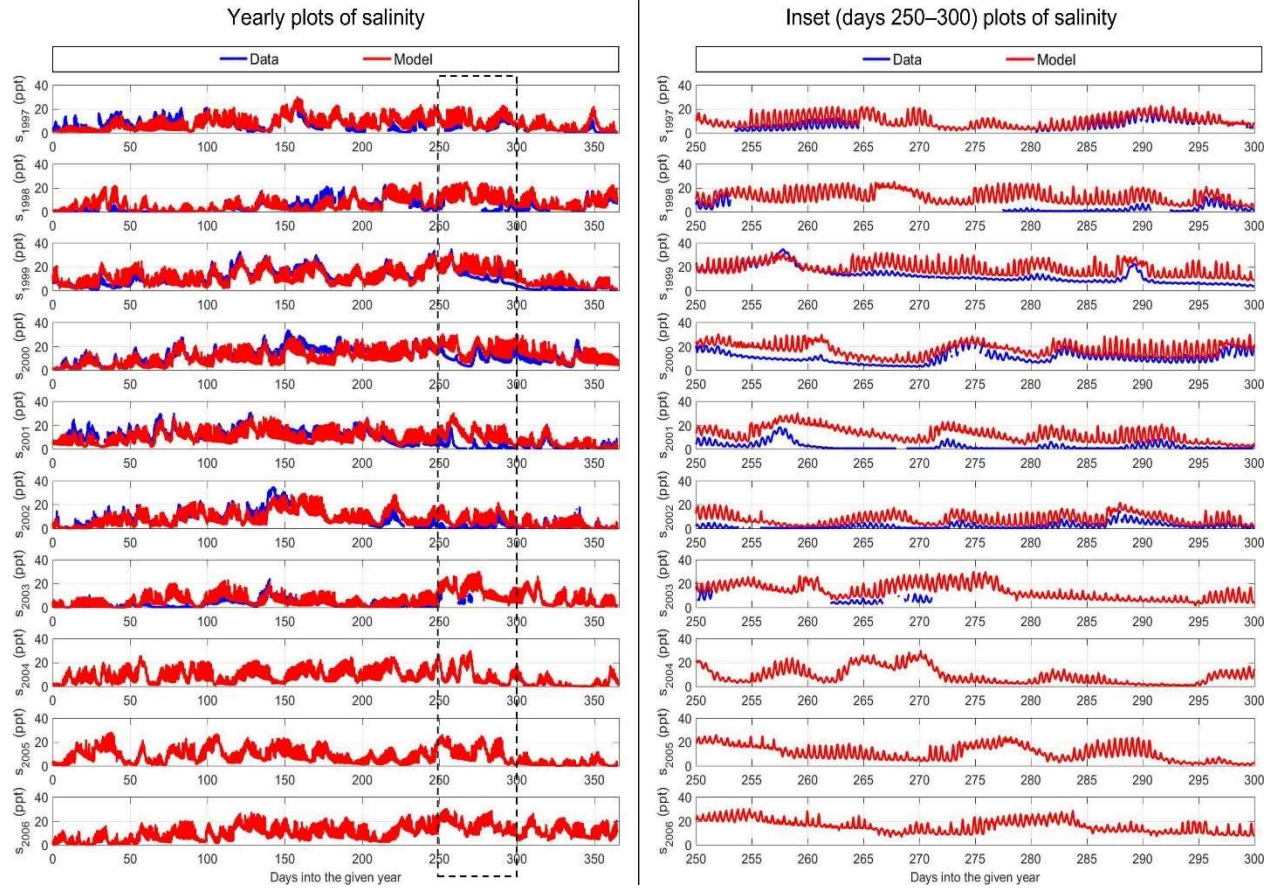


Figure 5. Time-series salinity records of data and model results at Acosta Bridge (river km 40)

for the 10-year record (1997–2007). The model results shown are from simulations with tributary inflows included in the model runs.

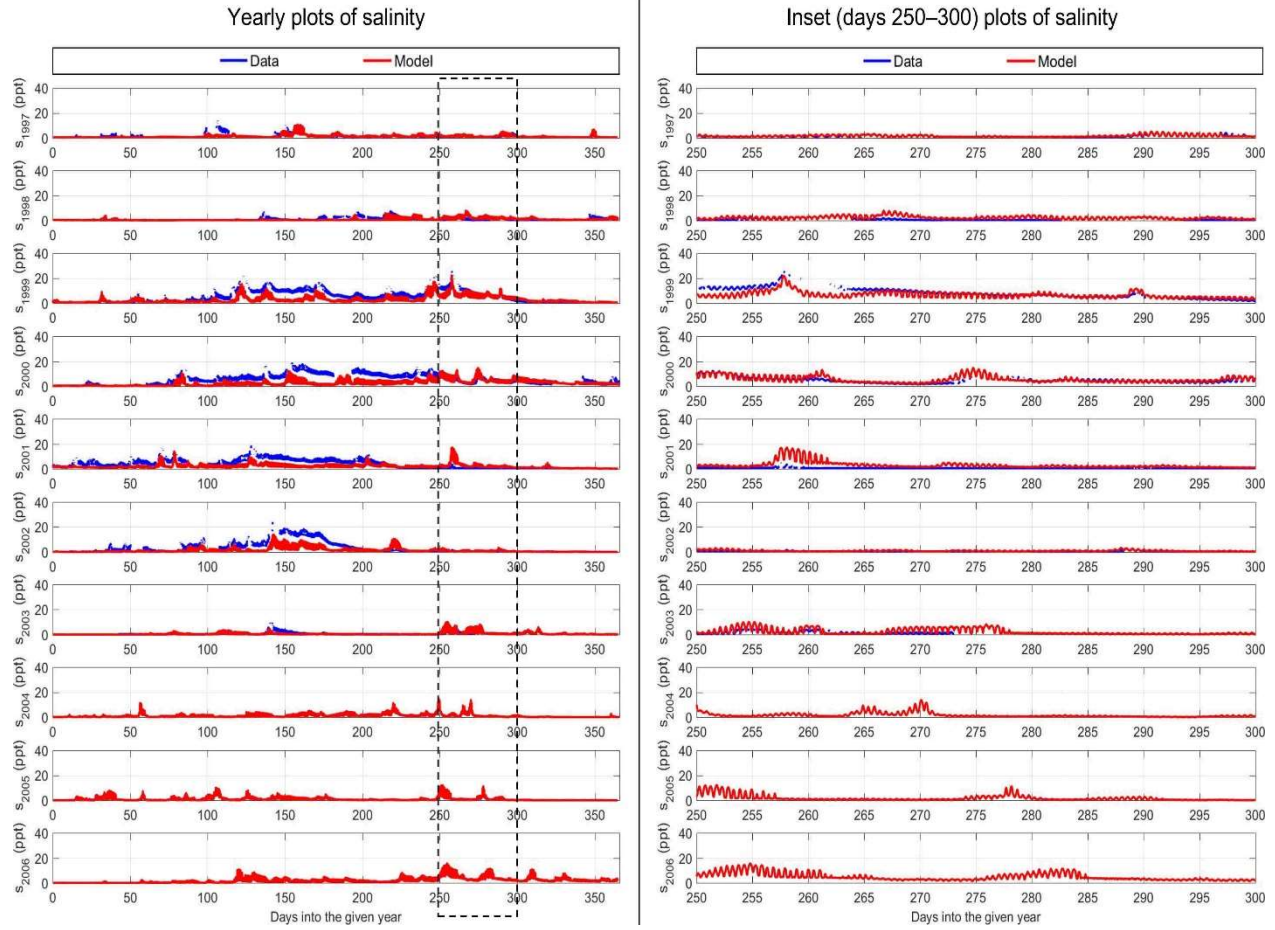


Figure 6. Time-series salinity records of data and model results at Buckman Bridge (river km 60) for the 10-year record (1997–2007). The model results shown are from simulations with tributary inflows included in the model runs.

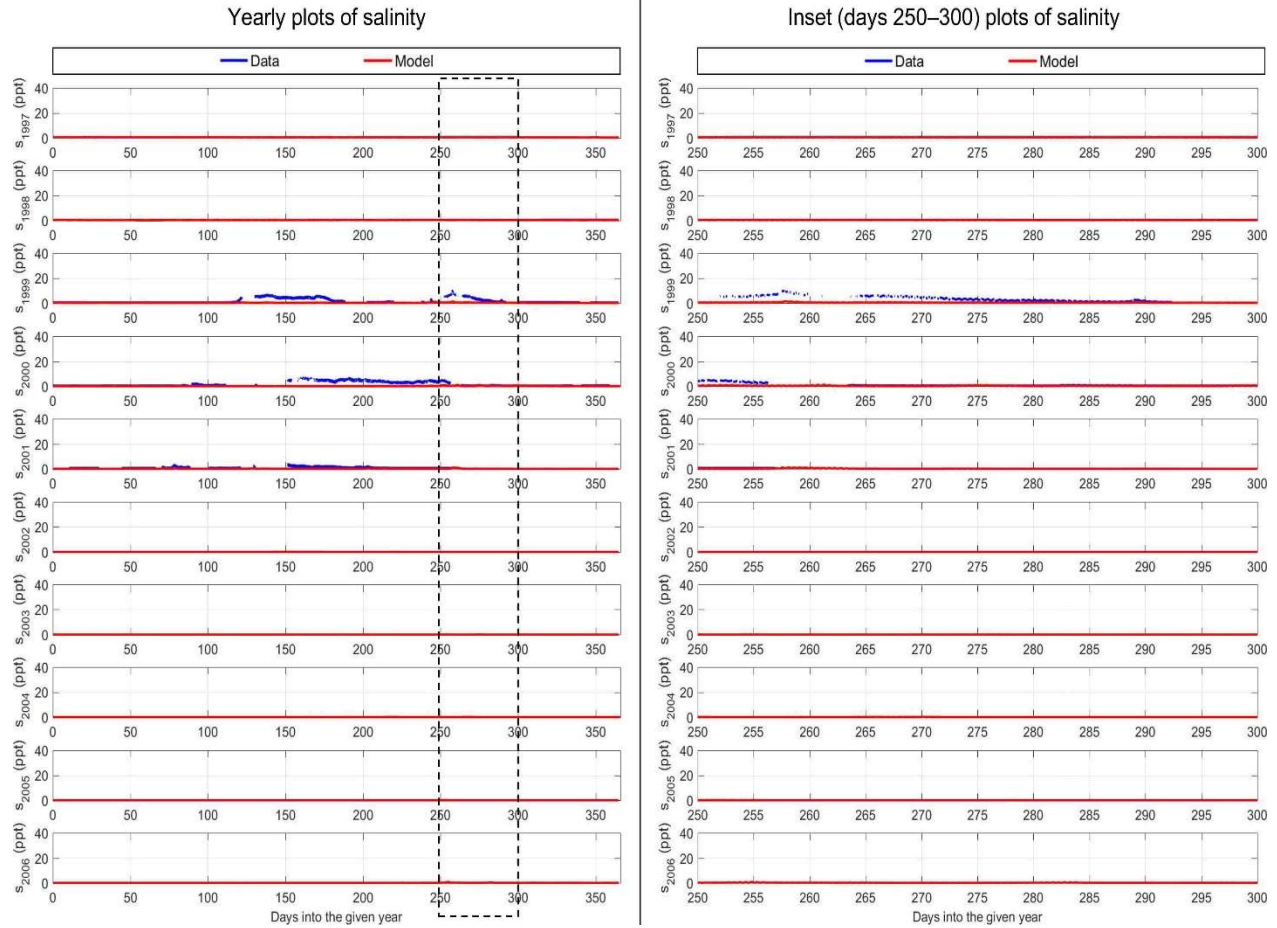


Figure 7. Time-series salinity records of data and model results at Shands Bridge (river km 80) for the 10-year record (1997–2007). The model results shown are from simulations with tributary inflows included in the model runs.

4.2. Distribution analysis and eigen-analysis

CDFs of salinity for the four salinity-gauging stations were generated from the data and simulated (i.e., Run 2; refer to Table 1) records, which are displayed in Figure 8. The longitudinal variation of salinity is shown by inter-comparing the CDFs among the four different stations (ranging from river km 20 to river km 80). The CDF at Dames Point is normal-like with most of the salinity values (~60%) contained in the 15–25 ppt range. The CDFs at Acosta Bridge, Buckman Bridge and Shands Bridge are gamma-like and progressively become more right-skewed with greater upriver distance. The numerical simulation replicates the distributions of the data at Dames Point with RMSE of 3.87% and IA of 1.00, and at Acosta Bridge, Buckman Bridge and Shands Bridge (RMSE's 4.53–8.23% and IA's 0.85–0.99).

The first and second eigenvalues obtained from the eigen-analysis of salinity records (data and model) represent 97.0 and 2.2%, respectively, of the space-time variability of salinity in the Lower St. Johns River. Figure 9 displays the PC values over the 200-km river length for the first (panel a) and second (panel e) PCs. The PC1 values range from -4000 to 0 over the entire river length. The PC2 values range from -500 to 500 and are roughly one order of magnitude less than the PC1 values. Salinity records were reconstituted (see Equation 12) based on the first and second PCs, where the statistics (mean and standard deviation) thereof are illustrated in Figure 9: the PC1 salinity signal contains the mean value plus a majority of the fluctuation about mean (panel c); while PC2 accounts for less than 0.2 ppt of the mean signal and at most 1–4 ppt of the signal variability (panel g). The PC1 salinity signal compares with the eigenanalysis input (i.e., Run 2) with RMSE of 0.09–4.10 ppt, SI of 0.11–0.70 and IA of 0.12–0.81, while the PC2 salinity signal (in addition to PC1) improved the error metrics (Table 2):

RMSE's 0.06–1.52 ppt; SI's 0.07–0.56; and IA's 0.23–0.93. It requires the first ten PCs to capture essentially all of the salinity signal ($SI = 0.01$) at Dames Point, while the first ten PCs capture the salinity signals at Acosta Bridge, Buckman Bridge and Shands Bridge with respective SI values of 0.04, 0.35 and 0.13. In order to capture approximately three-quarters ($IA = 0.75$) of the salinity signal, one would need just the first PC for Dames Point, the first two PCs for Acosta Bridge, the first five PCs for Buckman Bridge and the first ten PCs for Shands Bridge. The cyclical tide and generally more dynamic environment of the downstream parts of the river (e.g., Dames Point and Acosta Bridge) is the reason for the relatively few PCs required to regenerate the salinity signal there, while the low-energy and more episodic environment of the upstream parts of the river (e.g., Buckman Bridge and Shands Bridge) is the reason for the relatively large number of required PCs there.

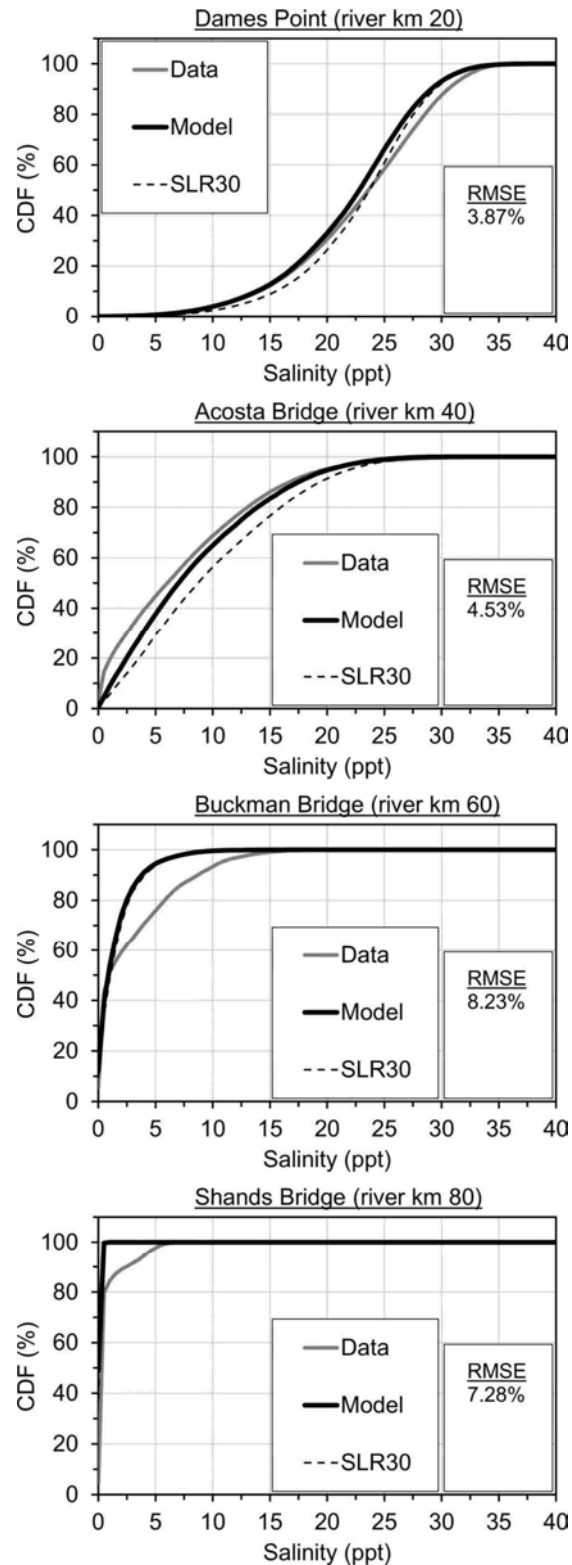


Figure 8. CDFs of salinity (data and model: present-day conditions—Run 2 and sea-level rise of 0.30 m—Run 10) for the four salinity-gauging stations located in the lower St. Johns River.

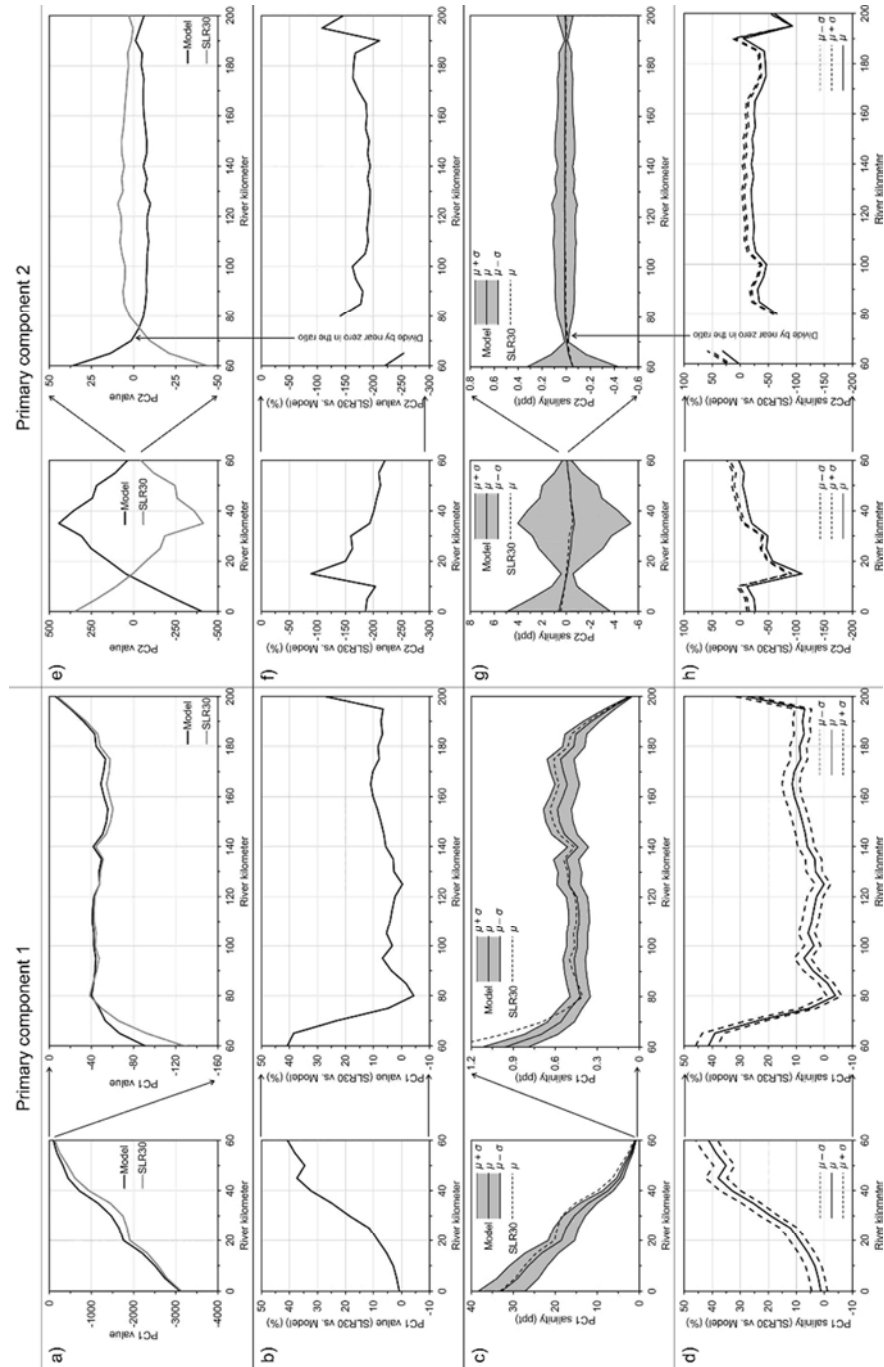


Figure 9. The eigen-analysis results are based on Runs 2 (present-day conditions—labeled as Model) and 10 (sea-level rise of 0.30 m—labeled as SLR30) and focus on the first two principal components (PCs): a/e) PC values; b/f) percent change of PC value due to sea-level rise; c/g) reconstituted salinity records (PC salinity); and d/h) percent change of PC salinity due to sea-level rise.

4.3. Model sensitivity with regard to salinity-field initial condition

The sensitivity analysis (model sensitivity to salinity-field initial condition) compares the model output from Runs 3–6 to that of Run 2 (control). The model sensitivity results are displayed in Figure 10 for the four salinity-gauging stations. The values shown are salinity ratios relative to the control run: $(S_{Runn} - S_{Run2}) \div S_{Run2}$ where $n = 3-6$. The salinity ratios begin at the prescribed error percentages of -10% , -5% , $+5\%$ and $+10\%$, respectively. The occurrence of dynamic equilibrium is defined as when (if) the given salinity ratio reaches 2% . At Dames Point, the curves begin to converge after 8 days, and the $\pm 5\%$ initial conditions dynamically equilibrate (reach the 2% threshold) after 41–55 days, while the $\pm 10\%$ initial conditions require 94–117 days to achieve dynamic equilibrium. Also, the negative-adjusted initial conditions dynamically equilibrated faster than the positive-adjusted initial conditions. At Acosta Bridge and Buckman Bridge, the curves begin to converge at 38 and 91 days, respectively, while afterward the curves converge to near 2% (dynamic equilibrium) after 6–9 months. At Shands Bridge, the curves converge almost immediately after the run begins, but afterward the curves remain separated and ultimately converge to no less than about half of the initial prescribed error value.

The recommendation is to use a data-based salinity field for the initial condition; however, if there is an error (within 10%) in the data and/or the incorporation of the data into the initial condition, then it is recommended to allow the model run enough time (2–4 months of simulation time, at minimum) for the salinity simulation to achieve dynamic equilibrium, whereby the simulation results thereafter are unaffected (or at least, less affected) by the error in

the initial condition. Special care should be taken in the prescription of the initial condition for low-salinity regions (Buckman Bridge and Shands Bridge), while there is more forgiveness for the moderate-/high-salinity regions (Dames Point and Acosta Bridge).

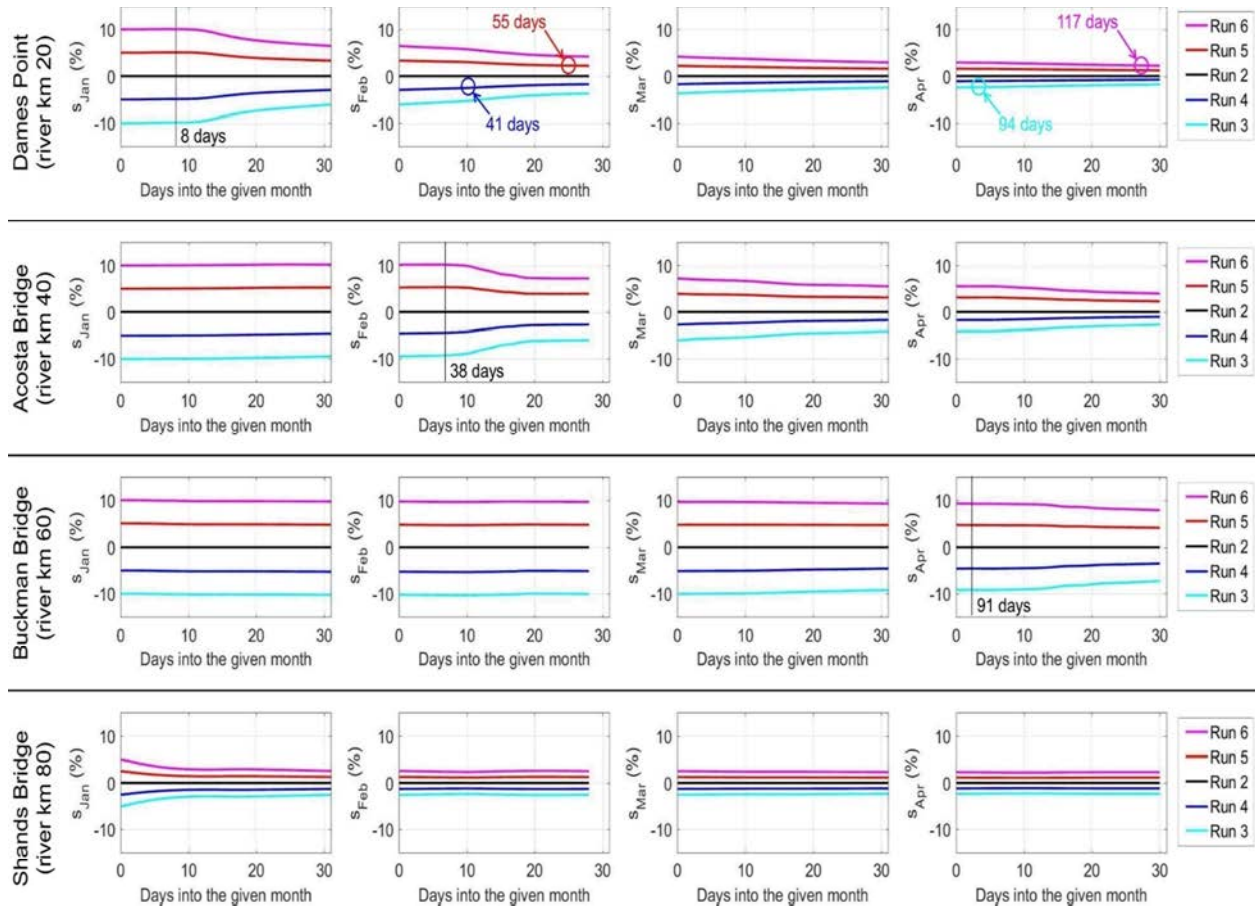


Figure 10. Salinity ratios ($s_{Run n} : s_{Run 2}$) based on Runs 2–6 for the four salinity-gauging stations located in the lower St. Johns River. For each station, there are four panels showing monthly (January, February, March and April) plots of salinity ratios for the start of the simulation (year 1997). The x -axis per plot is relative to the first day of the given month. The vertical lines indicate the start of convergence. The colored circles (Dames Point) represent when the given run converges to within the prescribed threshold of $\pm 2\%$. The annotations denoting number of days is in reference to January 1, 1997.

CHAPTER 5: ANALYSIS

5.1. Sea-level rise impacts

Simulation output from Runs 2 (control) and 7–10 were inter-compared among each other to analyze sea-level rise impacts on salinity in the lower St. Johns River and its tributaries. Runs 2, 7 and 8 were inter-compared to examine the system's present-day condition of salinity change over the sea-level scenarios of -0.05 , 0 and $+0.05$ m. Inter-comparison of runs 9 and 10 with Runs, 2 (control), 7 and 8 provides insight into salinity change for cases of more accelerated sea-level rise ($+0.15$ and $+0.30$ m).

5.1.1. Change of salinity as a function of sea-level rise

A first-order derivative, central difference approximation accurate to the second order was used to estimate the derivative of salinity change as a function of sea-level rise ($ds/d\delta$):

$$\left(\frac{ds}{d\delta}\right)_{\delta=0} = \frac{(s_{\delta=+5}) - (s_{\delta=-5})}{2\Delta|\delta|} \quad (13)$$

where s is salinity, δ is sea-level rise and the subscripts $\delta=+5$ and $\delta=-5$ denote the time-forward (sea-level rise of $+0.05$ m, i.e., Run 8 in Table 1) and time-backward (sea-level rise of -0.05 m,

i.e., Run 7 in Table 1) states of river/tributary salinity, respectively. Calculated in this manner, $ds/d\delta$ represents the linear trend (i.e., first derivative) of salinity change as a function of sea-level rise for present-day conditions, i.e., subscript $\delta=0$. The underlying concept of the analysis is to analyze whether $(ds/d\delta)_{\delta=0}$ provides insight into the how salinity in the river/tributaries is currently in a state of flux due to sea-level rise. The units of $ds/d\delta$ are ppt cm^{-1} , i.e., change in salinity per increment of sea-level rise, where positive values indicate increasing salinity and negative values indicate decreasing salinity. In addition, the first-order derivative approximation of $(ds/d\delta)_{\delta=0}$ computed here provides a basis (linear trend) to compare the results obtained from more accelerated cases of sea-level rise, i.e., +0.15 and +0.30 m, for an evaluation of nonlinear response. For a given location, salinity (s) is a function of time (i.e., hourly increment over 1997–2007), and thus, $(ds/d\delta)_{\delta=0}$ is a function of time. Herein, the notation $\| \|$ is used to denote the record-average value, i.e., $\|(ds/d\delta)_{\delta=0}\|$. Table 3 lists values of $\|(ds/d\delta)_{\delta=0}\|$ for the four salinity-gauging stations and 13 tributaries of the lower St. Johns River based on analysis of the 10-year record (1997–2007). The $\|ds/d\delta\|$ values range from +0.000 749 to +0.043 184 ppt cm^{-1} over the four salinity-gauging stations, and from +0.000 195 to +0.079 169 ppt cm^{-1} for the 13 tributaries, while all $\|ds/d\delta\|$ values are positive.

Curve fitting was applied (specifically, MATLAB `polyfit`) to the model results obtained from Runs 2 and 7–10 to generate a polynomial approximation of salinity versus sea-level rise:

$$s_{\text{poly}}(\delta) = p_1\delta^4 + p_2\delta^3 + p_3\delta^2 + p_4\delta + p_5 \quad (14)$$

where the p values are the polynomial coefficients and s_{poly} is a fourth-order polynomial since there are five data points of δ (i.e., -5, 0, 5, 15 and 30) used to construct s_{poly} . Emphasis is placed on p_5 , which is the constant term (units = ppt), p_4 , which is the linear-change term (units = ppt cm^{-1}), and p_3 , which is the first nonlinear-change term (units = ppt cm^{-2}). Positive p_4 and p_3 values indicate increasing salinity and negative p_3 and p_4 values indicate decreasing salinity. The

value of p_5 is used to normalize the changes in salinity captured in p_4 and p_3 , and thusly express the salinity change as a percentage. Table 3 lists values of p_4 , p_3 and p_5 for the four salinity-gauging stations and 13 tributaries of the lower St. Johns River based on analysis of the 10-year record (1997–2007). Firstly, the p_4 values are nearly equivalent to the $\|ds/d\delta\|$ values and positive for all locations. Secondly, the p_3 values are greatest at Acosta Bridge (+0.000 464 ppt cm⁻²) among the four salinity-gauging stations and at Broward River (+0.000 598 ppt cm⁻²) among the 13 tributaries. Thirdly, the p_3 value at Shands Bridge is negative (−0.000 008 ppt cm⁻²), and the p_3 values for Doctors Lake and the six tributaries located further upstream are negative and/or less than 10⁻⁵ ppt cm⁻² in magnitude.

Table 3

Values of $|(ds/d\delta)_{\delta=0}|$, p_4 , p_3 and p_5 for the four salinity-gauging stations and 13 pre-identified tributaries. See Equation (13) and (14) for reference.

Station	river km	$ (ds/d\delta)_{\delta=0} $	p_4	p_3	p_5
		ppt cm ⁻¹	ppt cm ⁻¹	ppt cm ⁻²	ppt
Dames Point	20	0.039 288	0.039 231	0.000 344	20.16
Acosta Bridge	40	0.043 184	0.043 139	0.000 464	7.07
Buckman Bridge	60	0.004 336	0.004 328	0.000 109	1.08
Shands Bridge	80	0.000 749	0.000 751	−0.000 008	0.37
Timucuan Preserve	10	0.017 811	0.017 911	0.000 203	23.72
Intracoastal Waterway	10	0.010 247	0.009 762	0.000 400	21.74
Broward River	30	0.002 684	0.001 613	0.000 598	19.76
Trout River	35	0.040 926	0.040 313	0.000 551	15.52
Arlington River	35	0.079 169	0.079 014	0.000 505	11.27
Ortega River	45	0.002 958	0.002 961	0.000 026	1.88
Doctors Lake	65	0.000 195	0.000 196	0.000 002	0.08
Julington Creek	65	0.016 544	0.016 498	−0.000 322	1.36
Black Creek	70	0.000 467	0.000 470	−0.000 012	0.20
Sixmile Creek	85	0.000 825	0.000 817	−0.000 005	0.22
Deep Creek	115	0.000 700	0.000 716	0.000 001	0.37
Rice Creek	130	0.000 621	0.000 612	0.000 002	0.23
Dunn Creek	150	0.001 139	0.001 168	0.000 000	0.30

The polynomial fit of salinity (i.e., s_{poly} ; refer to (14)) was used to generate linear (i.e., summation of terms p_5 and p_4) and nonlinear (i.e., summation of terms p_5 , p_4 and p_3) approximations of salinity change due to sea-level rise (Figure 11). The x -axis ranges over the

four sea-level rise scenarios (and present-day conditions) investigated in the study. The left y -axis of each plot is the absolute change in salinity due to sea-level rise, and the right y -axis is the absolute salinity change normalized by the record-average value (p_5) of present-day salinity, multiplied by 100 to express the salinity change as a percentage. There is little to no difference between the nonlinear and linear salinity change for mild sea-level rise (+0.05 m); however, the nonlinear-linear difference is noticeable for moderate sea-level rise (+0.15 m) and appreciable for accelerated sea-level rise (+0.30 m). The nonlinear-linear difference is greatest (as much as 6–9%) for the two middle stations (Acosta Bridge and Buckman Bridge) and relatively much smaller (as much as 1%) for the downstream and upstream stations (Dames Point and Shands Bridge). Lastly, the nonlinear-linear difference is negative for Shands Bridge.

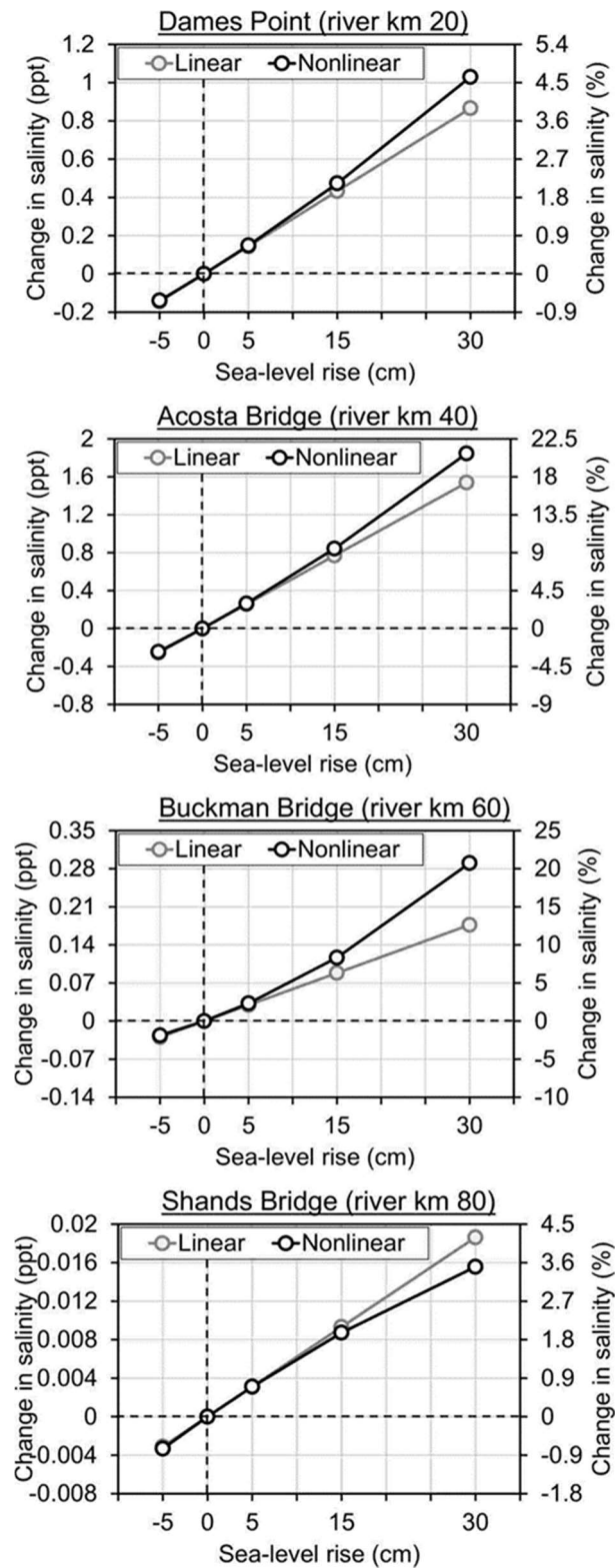


Figure 11. Linear and nonlinear change in salinity due to sea-level rise for the four salinity-gauging stations located in the lower St. Johns River.

Linearity implies the change over the previous step will be the same going into the future. Nonlinearity acts to otherwise adjust the linear curve upward or downward. Numerous studies have emphasized nonlinear hydrodynamic/flooding changes due to sea-level rise (e.g., see (Bilskie et al., 2016) for an example dealing with the northern Gulf of Mexico); however, this study is the first of its kind to demonstrate the linear-versus-nonlinear response of salinity in a coastal river due to sea-level rise. The linear-nonlinear response is further explored in two ways: 1) what is the direction of nonlinearity over the 200-km length of the lower St. Johns River; and 2) what is the magnitude of the nonlinearity? Values of p_4 , p_3 and p_5 (see Equation 14) were computed for the 41 river-axis stations. The ratio of $p_4:p_5$ represents the linear salinity change relative to the present-day state (average) of salinity. The signage (+/−) of p_3 indicates the direction of nonlinearity and the absolute value of p_3 indicates the magnitude of nonlinearity. Additionally, values of cumulative volumetric flow per unit width were computed for the 41 river-axis stations:

$$q_{\text{cum}}(x_j) = h(x_j)(\Delta t) \sum_{n=1}^N V_n(x_j, t_n), \quad j \in 1 \dots 41 \quad (15)$$

where q_{cum} has units of $\text{m}^3 \text{m}^{-1}$ and is a profile of values for the 41 river-axis stations (x is river distance of 0–200 km at 5-km increment), h is the local bathymetric depth, Δt is the time step (hourly), V_n is the time-dependent, along-channel velocity, n is the time counter and N is the total number of time counts. Positive q_{cum} values indicate local estuary infilling (i.e., flood dominance) and negative q_{cum} values indicate local estuary flushing (i.e., ebb dominance). The change in q_{cum} due to sea-level rise is the focus herein: $\Delta q_{\text{cum}} = q_{\text{cum}}|_{\delta=30} - q_{\text{cum}}|_{\delta=0}$. Δq_{cum} is used as a measure of the change in cumulative volumetric flow within the river due to sea-level rise.

The notion is that positive Δq_{cum} represents the local infilling of saline waters due to the sea-level rise, and the opposite case for negative Δq_{cum} .

Figure 12 shows values of p_4 , $p_4:p_5$, p_3 and Δq_{cum} computed for the 200-km length of the lower St. Johns River. The values of p_4 and $p_4:p_5$ are positive over the full 200-km river length, which is suggestive of increasing salinity in the lower St. Johns River due to sea-level rise. Although the p_4 values peak at river km 30, there are multiple peaks in the $p_4:p_5$ values (river locations 45, 95, 105, 140, 160 and 185 km). The p_4 and $p_4:p_5$ values reach local minima at river km 80, whereas the p_4 values upstream thereof remain very small ($< 0.002 \text{ ppt cm}^{-1}$) and the $p_4:p_5$ values upstream of river km 95 progressively decay from $\sim 0.5 \% \text{ cm}^{-1}$ in terms of magnitude. The p_3 values peak at river km 35 and are negative or slightly positive ($< 0.2 \text{ ppt cm}^{-2}$) after river km 80. The Δq_{cum} values peak at river km 20 ($+3.1 \times 10^6 \text{ m}^3$), reach a local minimum at river km 40 ($-2.4 \times 10^6 \text{ m}^3$) and are generally negative upstream of river km 80. The peak Δq_{cum} value at river km 20 and local minimum Δq_{cum} value at river km 40 enclose the peak p_3 value at river km 35, indicating there is a local “hotspot” in the lower St. Johns River where salinity will increase nonlinearly because of local infilling of saline waters due to sea-level rise. The generally negative Δq_{cum} values upstream of river km 80 are collocated with the negative or slightly positive ($< 0.2 \text{ ppt cm}^{-2}$) p_3 values, such that the upper parts of the lower St. Johns River will become more ebb-dominated due to sea-level rise and the associated salinity change will be positive on an overall basis, positive on a linear basis and negative on a nonlinear basis.

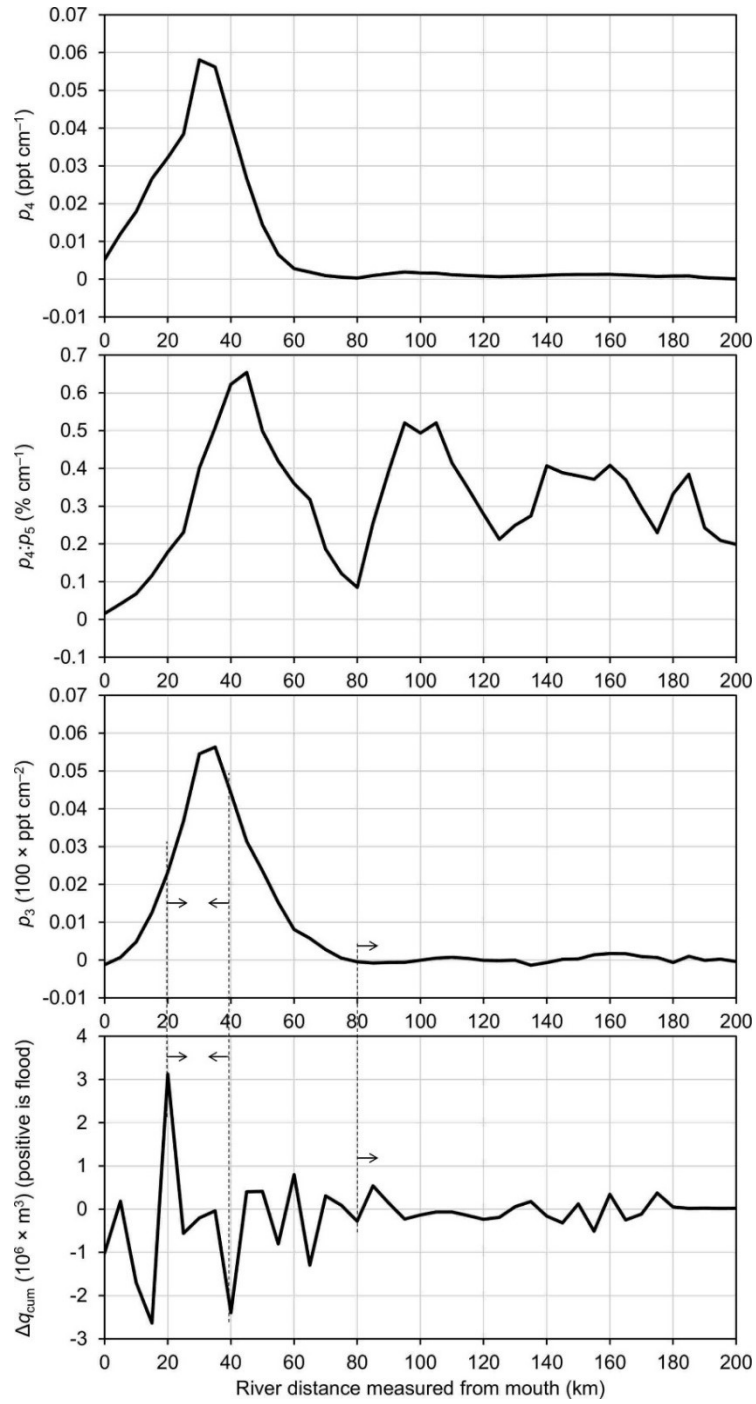


Figure 12. Plots for the 200-km length of the lower St. Johns River, including values of: a) p_4 ; b) $p_4:p_5$; c) p_3 ; and d) Δq_{cum} . The vertical dashed lines are for reference as related to the discussion in the text.

5.1.2. Distribution analysis and eigen-analysis

The CDFs of salinity will shift due to sea-level rise. This is displayed in Figure 8 where the CDFs shift to the right, which suggests an increase in salinity. The CDF at Dames Point shifts to the right in the plot essentially over the full distribution, particularly in the salinity zone of 20-35 ppt, which is indicative of increasing salinity by 1–5 ppt. The CDF at Acosta Bridge becomes more so flattened over the full distribution, including a shift to the right, which causes an increase in salinity by 2–4 ppt. Although indistinguishable in the plots, the CDFs for Buckman Bridge and Shands Bridge also shift to the right (i.e., increasing salinity).

The PCs of salinity will adjust as a result sea-level rise, as shown in Figure 9. The PC1 values increase in magnitude over almost the entire river length and especially so (10-40%) for river km's 20–70 (panels a and b); and the PC2 values become flipped with regard to signage and increase in magnitude over the entire river length by a factor of 1 – 2 (panels e and f). The PC adjustments due to sea-level rise have the following impacts on salinity in the river (Figure 9): PC1 salinity increases on a mean basis (μ) by 1–2 ppt (10–40%) for river km's 20–70, while the lower bound ($\mu - \sigma$) of the salinity range will increase more than that of the upper bound ($\mu + \sigma$) (panels c and d); and PC2 salinity goes up and down by 0.02–0.05 ppt (within ~100%) over the entire river length (panels g and h).

5.2. Implications on estuarine biology

The results can be useful for river management projects to provide information on long-term salinity conditions in the river, relative to present-day conditions, and the associated biological shifts that would be expected to take place. For instance, where will river biota migrate to sustain against changes in the salinity due to sea-level rise? To provide an example extension of the results, salinity tolerances were gathered for 81 species identified in the lower St. Johns River. Salinity tolerance can be expressed in two dimensions, as illustrated in Figure 13 for the 81 river species: average basis, which has limits of fresh (low average salinity) and saline (high average salinity); and range (i.e., standard deviation) basis, which has limits of sensitive (low standard deviation salinity) and tolerant (high standard deviation salinity). The average value denotes the optimal level of salinity preferred by the given species, and the standard deviation value denotes the range of salinity levels tolerated by the given species. The model results for the 41 river-axis stations, i.e., statistics derived from them, including average and standard deviation, were compared with the species-based salinity tolerances (average and standard deviation) to estimate the optimal location and longitudinal range in the river of the 81 species. Average salinity conditions in the river were compared with the average value of the species-preferred salinity to determine the species' optimal location in the river, while the lower limit of the salinity conditions in the river (i.e., average minus standard deviation) was compared with the upper-limit salinity tolerance (i.e., average plus standard deviation) per species to identify the species' upper limit of the river-longitudinal range, and vice versa. The analysis was applied to the model results for Runs 2 and 10 (Table 1) to generate historical and future conditions, respectively, of the species' locations (optimal and range) in the river. Species

migration due to sea-level rise (and the associated increase in salinity) was calculated as the future-versus-historical change in species location (optimal and range) in the river.

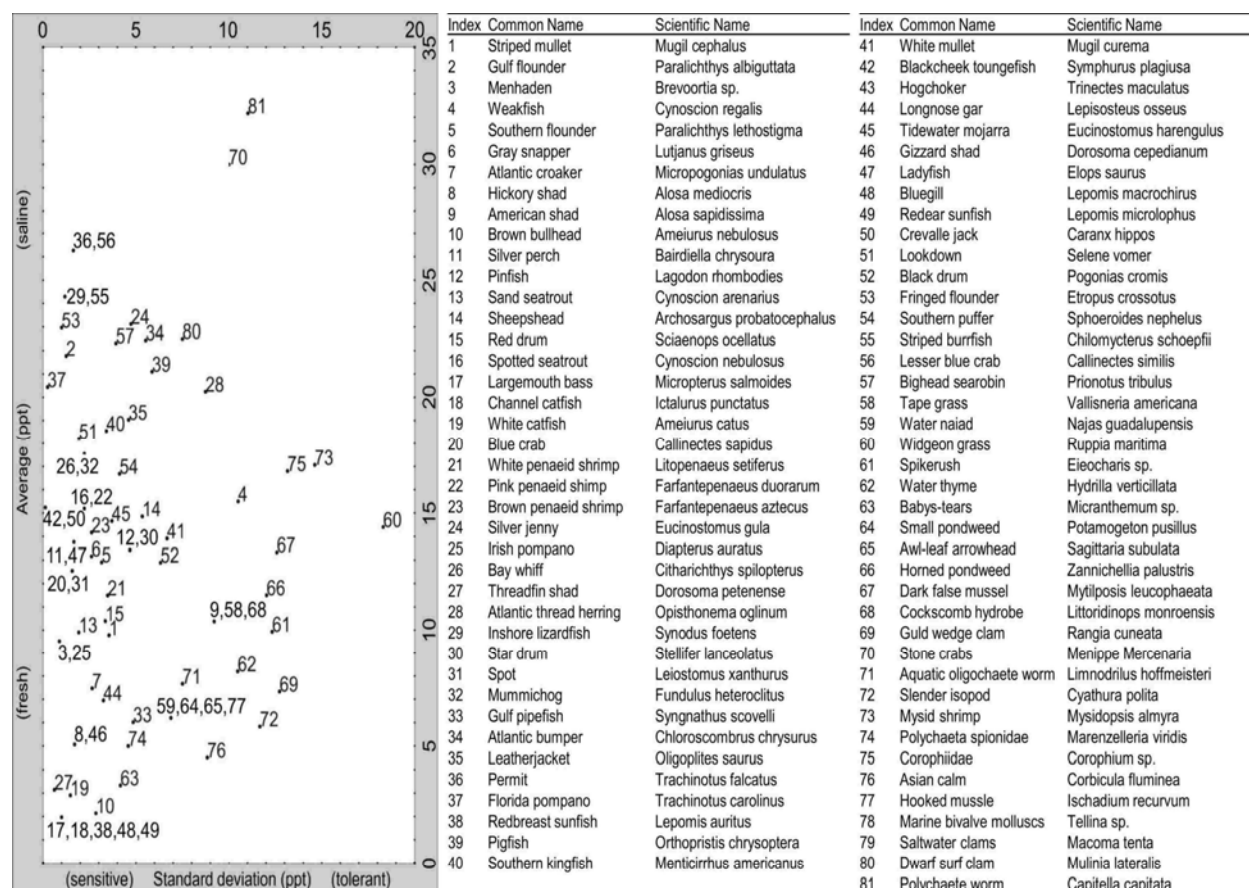


Figure 13. A total of 81 species are defined in terms of salinity tolerance, including average and standard deviation.

Figure 14 shows the salinity tolerance (optimal and range), location in the river (optimal and range) for present-day conditions and migration (change in optimal and range of location—future versus historical) due to sea-level rise / increasing salinity for the 81 species. The percentage value of migration is the absolute value of migration normalized by the present-day location (optimal) of the given species. Migration is positive for all species in the lower St. Johns River, except for one (index 57) stable species (bighead sea robin) where migration is zero. The greatest impact of increasing salinity due to sea-level rise is for the species located in the lower 40 km of the St. Johns River. Species migration is in the general range of 1.5–3 km, which corresponds to a 5–10% change relative to its present-day location. Some examples of species

migration include: blue crabs (index 20) will migrate upriver by 1.67 km (6%); bait shrimp (22/23) 1.86 km (7%); stone crabs (70) 1 km (3%); striped mullet (1) 2 km (6%); flounder (2) 2 km (13%); red drum (15) 2.33 km (8%); spotted sea trout (16) 1.67 km (7%); croaker (7) 1.67 km (5%); sheepshead (14) 2.33 km (10%); largemouth bass (17) 2.33 km (5%); and blue gill (48) 2.33 km (4%). Of course, there are biological dynamics that would occur and the approximation of species migration showed here is just an example extension of the salinity model results; however, this application demonstrates the potential for coupling of hydrodynamic-salinity models with ecological-biological models for practical, yet scientific, prediction of environmental changes due to sea-level rise.

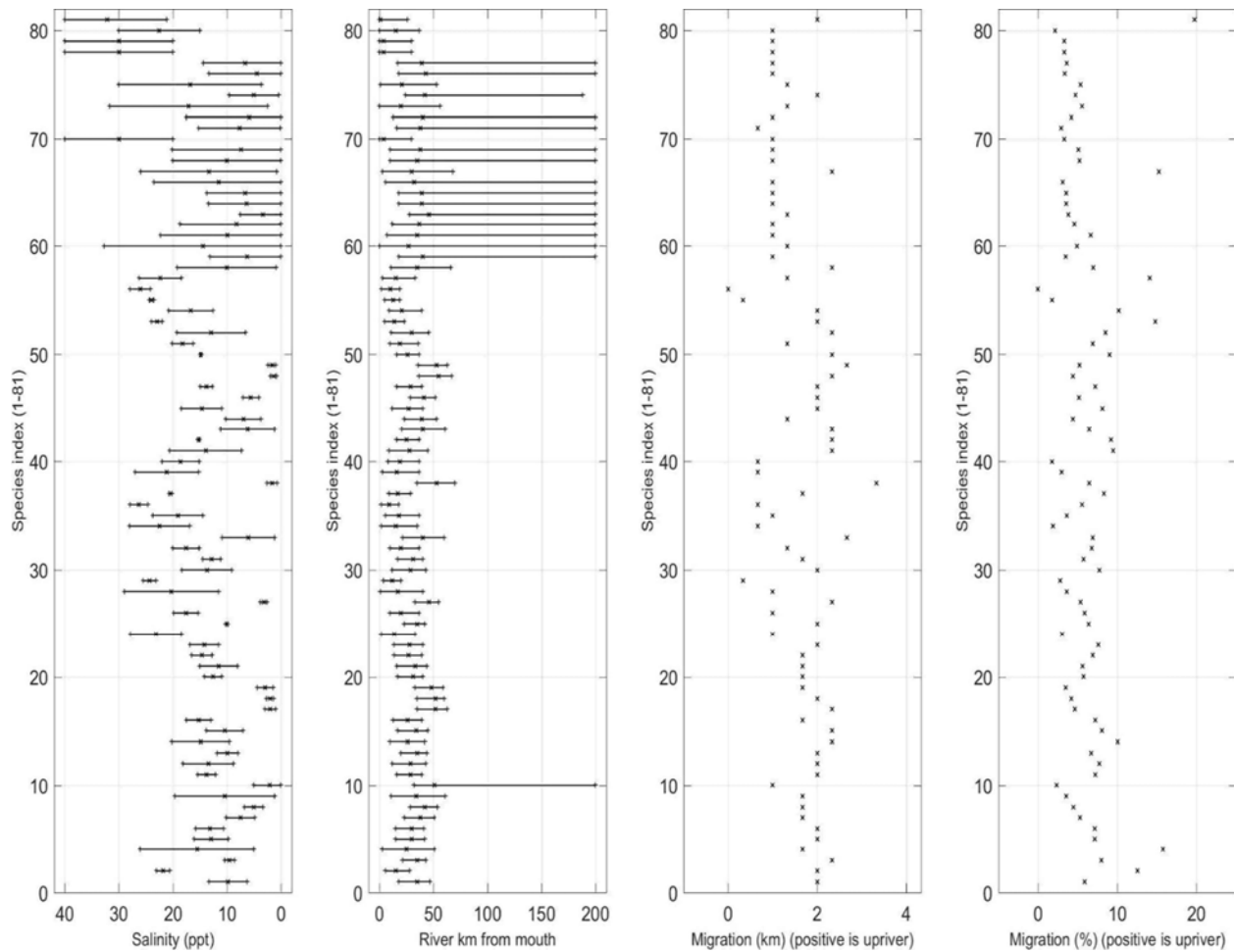


Figure 14. Salinity tolerance, location in the river for present-day conditions and migration (change in river location) due to sea-level rise / increasing salinity for the 81 species.

CHAPTER 6: CONCLUSIONS

Numerical simulation of salinity (DG-SWEM: discontinuous-Galerkin, shallow-water equations model) in the lower St. Johns River (northeastern Florida, USA) was accomplished for an unprecedented, contiguous run length of ten years (1997–2007). Boundary conditions consisted of continuous data, including offshore water level, upstream river inflow and tributary inflows (nine in total). The model was validated against salinity data for four gauging stations located at 20, 40, 60 and 80 km upriver with root mean square error of 1.49–5.34 ppt and index of agreement (analogous to R^2) of 0.34–0.83. The model validation demonstrated the relative importance of including tributary inflows (in addition to upstream river inflows) in the salinity simulation. Although upstream river inflow provides the dominant volumetric flux of freshwater into the river and is a controlling factor of river-wide salinity, the distributed inflow derived from the tributaries impacts salinity in the river locally and for only short durations. The next logical step would be to integrate the existing hydrodynamic-transport model (DG-SWEM) with a hydrologic component that fully encompasses the watershed-derived rainfall runoff. The initial condition of salinity used to start the simulation needs to be based on available salinity data, which in this case was supplied by the four salinity-gauging stations in the river. Assumptions of saline-water conditions (35 ppt) and freshwater conditions (0.2 ppt) can be made for the offshore and upstream model boundaries, respectively; however, it is critical that the model's interior of

the salinity-field initial condition reflect the actual timestamped salinity in the river. Error in the initial condition should

be kept to within $\pm 10\%$ of available data to ensure that the simulation will equilibrate to a common dynamic salinity state, where it requires 6–9 months for uncertainty in the initial condition to be inconsequential to the simulated time-series salinity.

Salinity will increase over the entire 200-km length of the lower St. Johns River due to sea-level rise. In general, risen offshore water levels will enable more saline waters to flux into the river, while subsequently pushing back on the freshwater discharge coming down from upriver, which together will cause salinity in the river to increase. The salinity increase will be spatially variable over the river's length, where the greatest change in salinity will occur around river km 40, with a derivative valued at 0.06 ppt cm^{-1} , and lower-valued derivatives of salinity change will occur at the river mouth and upstream of river km 60. Although the derivatives of salinity increase for river km's 80–200 are near nil on an absolute basis, they are non-negligible when compared with the present-day condition of salinity ($0.2\text{--}0.5\% \text{ cm}^{-1}$). The nonstationarity of salinity in the river due to sea-level rise is further explained by changes in probability distributions (shape and translation) and eigen-based principal components (shifts and reflections). The salinity increase will be nonlinear, particularly for scenarios of moderate to accelerated sea-level rise ($0.15\text{--}0.30 \text{ m}$). The nonlinearity will intensify the salinity increase, especially for river km's 20–40, where there is a local “hotspot” in the river where salinity will increase nonlinearly (greater than the linear trend) due sea-level rise. For the case of accelerated sea-level rise (0.30 m), salinity at river km 40 will increase by close to 2 ppt, which corresponds to a greater-than-20% increase in salinity from present-day conditions.

The modeling approach used in this study is able to simulate changes in salinity due to sea-level rise, but there are assumptions made that limit the modeling approach. The finite element mesh is kept constant, which ignores any geomorphological evolution of the river due to

sedimentation and erosion. The upstream and tributary inflows are kept constant, which ignores any long-term changes of land use / land cover of the watershed and any climate variability of the precipitation. The offshore water level record (1997–2007) is assumed to be the same in the future (2047–2057), while there would be changes in the storm tide due to meteorological evolution over the 50-year period. The “variable” of the modeling approach is sea-level rise, as applied to the offshore water level record (i.e., 1997–2007 → 2047–2057). All other factors considered to remain the same, the modeling approach simulates changes in salinity due to sea-level rise.

Increased salinity in the lower St. Johns River due to estimated sea-level rise are expected to impact river biota by causing them to migrate further upriver by 1–3 km. Species currently located in the lowest 60 km of the river will migrate the most, since the salinity increase there is largest on a percentage basis, i.e., future-versus-historical salinity relative to historical salinity. Such a mapping of species migration can facilitate the prediction of organism life stages, e.g., alterations in recruitment locations in the river, and biological interactions, e.g., adjustments in interdependencies (predator-prey), likely to occur in the future.

Although a specific model (DG-SWEM) is applied to an individual estuary (lower St. Johns River) herein, the modeling approach is general for any numerical model and extensible to other estuaries. The ingredients needed to apply the modeling approach to other estuaries include: highly resolved, well-vetted mesh or grid of the domain; accurate offshore boundary conditions; upstream river-inflow boundary conditions; tributary-inflow boundary conditions; and data-based salinity field for initial condition. Regarding inflow boundary conditions, particular care should be given to capturing the full hydrologic input entering the estuary. The modeling approach is applicable to mesotidal and macrotidal estuaries (provided they are well-

mixed vertically), including fjord, bay, river and barrier-island systems, while it may breakdown for microtidal estuaries, particularly large and shallow lagoons, because of evaporative effects not being included.

LIST OF REFERENCES

- ADCIRC. (2016). The official ADCIRC website. Retrieved from <http://adcirc.org>
- Alizad, K., Hagen, S. C., Morris, J. T., Bacopoulos, P., Bilskie, M. V, Weishampei, J. F., & Medeiros, S. C. (2016). A coupled, two-dimensional hydrodynamic-marsh model with biological feedback. *Ecological Modelling* 327, 29–43.
- Baart, F., von Koningsveld, M., & Stive, M. J. F. (2012). Trends in sea-level trend analysis. *Journal of Coastal Research* 28, 311–315.
- Bacopoulos, P., Funakoshi, Y., Hagen, S. C., Cox, A. T., & Cardone, V. J. (2009). The role of meteorological forcing on the St. Johns River (northeastern Florida). *Journal of Hydrology* 369, 55–70.
- Bacopoulos, P., & Hagen, S. (2009). Tidal simulations for the Loxahatchee River estuary (southeastern Florida): On the influence of the Atlantic Intracoastal Waterway versus the surrounding tidal flats. *Journal of Waterway, Port, Coastal, and Ocean Engineering* 135, 259–268.
- Bacopoulos, P., & Hagen, S. C. (2014). Dynamic Considerations of Sea-level Rise with Respect to Water Levels and Flooding in Apalachicola Bay. *Journal of Coastal Research* 68, 43–48.
- Bacopoulos, P., Hagen, S. C., Cox, A. T., Dally, W. R., & Bratos, S. (2012). Observation and simulation of winds and hydrodynamics in St. Johns and Nassau Rivers. *Journal of*

Hydrology 420-421, 391–402.

Bacopoulos, P., Kubatko, E. J., Hagen, S. C., Cox, A. T., & Mulamba, T. (2016). Modeling and data assessment of longitudinal salinity in a low-gradient estuarine river. *Environmental Fluid Mechanics* 16, doi: 10.1007/s10652-016-9486-8. <http://doi.org/10.1007/s10652-016-9486-8>

Bergman, M. J. (1992). Volume 2 of the St. Johns River reconnaissance: Surface water hydrology. Technical Report SJ92-1, St. Johns River Water Management District.

Bilskie, M. V, Hagen, S. C., Alizad, K., Medeiros, S. C., Passeri, D. L., Needham, H. F., & Cox, A. T. (2016). Dynamic simulations and numerical analysis of hurricane storm surge under sea level rise with geomorphologic changes along the northern Gulf of Mexico. *Earth's Future*, doi: 10.1002/2015EF000347.

Bilskie, M. V, Hagen, S. C., Medeiros, S. C., & Passeri, D. L. (2013). Dynamics of sea level rise and coastal flooding on a changing landscape. *Journal of Geophysical Research (Oceans)* 41, doi: 10.1002/2013GL058759.

Bunya, S., Dietrich, J. C., Westerink, J. J., Ebersole, B. A., Smith, J. M., Atkinson, J. H., ... Roberts, H. J. (2010). A High-Resolution Coupled Riverine Flow , Tide , Wind , Wind Wave , and Storm Surge Model for Southern Louisiana and Mississippi . Part I : Model Development and Validation. *Monthly Weather Review* 138, 345–377.

Church, J. A., & White, N. j. (2006). A 20th century acceleration in global sea-level rise. *Journal of Geophysical Research (Oceans)* 33, doi: 10.1029/2005GL024826.

Donnelly, J. P., & Bertness, M. D. (2001). Rapid shoreward encroachment of salt marsh

- cordgrass in response to accelerated sea-level rise. *Proceedings of the National Academy of Sciences* 98, 14218–14223.
- French, J. R. (2008). Hydrodynamic Modelling of Estuarine Flood Defence Realignment as an Adaptive Management Response to Sea-Level Rise. *Journal of Coastal Research* 24, 1–12.
- Friedrichs, C. T., Aubrey, D. G., & Speer, P. E. (1990). Impacts of relative sea level rise on evolution of shallow estuaries. In: Cheng, R.T. (ed.). *Residual Current and Long-term Transport*. Springer-Verlag, New York.
- Hagen, S. C., & Bacopoulos, P. (2012). Coastal Flooding in Florida's Big Bend Region with Application to Sea Level Rise Based on Synthetic Storms Analysis. *Terrestrial, Atmospheric and Oceanic Sciences Journal* 23, 481–500.
- Hagen, S. C., M.ASCE, Morris, J. T., Bacopoulos, P., M.ASCE, & Weishampei, J. F. (2012). Sea-Level Rise Impact on a Salt Marsh System of the Lower St. Johns River. *Journal of Waterway, Port, Coastal, and Ocean Engineering* 139, 118–125.
- Halpin, P. M. (2000). Habitat use by an intertidal salt-marsh fish: trade-offs between predation and growth. *Marine Ecology Progress Series* 198, 203–214.
- Henrie, K., & Valle-Levinson, A. (2014). Subtidal variability in water levels inside a subtropical estuary. *Journal of Geophysical Research (Oceans)* 119, doi: 10.1002/2014JC009829.
- Jevreieva, S., Moore, J. C., & Grinsted, A. (2010). How will sea level respond to changes in natural and anthropogenic forcings by 2100? *Geophysical Research Letters* 37, L07703.
- JU/UNF. (2016). The state of the river report for the lower St. Johns River basin. Florida.
- Kolar, R. L., Westerink, J. J., Gray, W. G., & Jr., L. R. A. (1994). Shallow water modeling in

spherical coordinates: Equation formulation, numerical implementation, and application. *Journal of Hydraulic Research* 32, 3–24.

Kubatko, E. J., Bunya, S., Dawson, C., Westerink, J. J., & Mirabito, C. (2009). A performance comparison of continuous and discontinuous finite element shallow water models. *Journal of Scientific Computing* 40, 315–339.

Kubatko, E. J., Dawson, C., & Westerink, J. J. (2008). Time step restrictions for Runge-Kutta discontinuous Galerkin methods on triangular grids. *Journal of Computational Physics* 227, (23), 9697–9710.

Kubatko, E. J., Westerink, J. J., & Dawson, C. (2006). hp discontinuous Galerkin methods for advection dominated problems in shallow water flow. *Computer Methods in Applied Mechanics and Engineering* 196, 437–451.

Livingston, R. J. (1991). Editor. *Rivers of Florida*, Ecological Studies 83. Springer-Verlag.

Luetlich Jr., R. A., Westerink, J. J., & Scheffner, N. W. (1992). An Advanced Three-dimensional Circulation Model for Shelves, Coasts, and Estuaries, I – Theory and Methodology of ADCIRC-2DDI and ADCIRC-3DL. Technical Report DRP-92-6.

Monahan, A. H., Fyfe, J. C., Ambaum, M. H. P., Stephenson, D. B., & North, G. R. (2009). Empirical orthogonal functions: the medium is the message. *Journal of Climate* 22, 6501–6514.

Morris, F. W. (1995). Volume 3 of the Lower St. Johns River basin reconnaissance: Hydrodynamics and Salinity. Technical Report SJ95-9, St. Johns River Water Management District.

- Murphy, A. H. (1988). Skill scores based on the mean square error and their relationship to the coefficient. *Monthly Weather Review* 116, 2417–2424.
- NOAA NOS. (2016). Center for Oceanographic Products and Services. Retrieved from <http://tidesandcurrents.noaa.gov/>
- Nyman, J. A., DeLaune, R., Roberts, H., & Patrick Jr, W. H. (1993). Relationship between vegetation and soil formation in a rapidly submerging coastal marsh. *Marine Ecology Progress Series (Oldendorf)* 96, 269–279.
- Passeri, D. L., Hagen, S. C., Medeiros, S. C., & Bilskie, M. V. (2015). Impacts of historic morphology and sea level rise on tidal hydrodynamics in a microtidal estuary (Grand Bay, Mississippi). *Continental Shelf Research* 111, 150–158.
- Pennings, S. C., & Bertness, M. D. (2001). Salt marsh communities. *Marine Community Ecology*, 289–316.
- Shellenbarger, G. G., & Schoellhamer, D. H. (2011). Continuous salinity and temperature data from San Francisco estuary, 1982-2002: Trends and salinity-freshwater inflow relationship., 1191–1201.
- SJRWMD. (2016). Online Tools, GIS, Data. Retrieved from www.sjrwmd.com/toolsGISdata
- Sucsy, P. V., & Morris, F. W. (2002). Calibration of a Three-dimensional Circulation and Mixing Model of the Lower St. Johns River. Technical Memorandum Draft 1.1, St. Johns River Water Management District.
- Toth, D. (1993). Volume 1 of the Lower St. Johns River reconnaissance: Hydrogeology. Technical Report SJ93-7, St. Johns River Water Management District.

U.S. Geological Survey. (2013). "Potential Effects of Deepening the St. Johns River Navigation Channel on Saltwater Intrusion in the Surficial Aquifer System, Jacksonville, Florida."

U.S. Geological Survey. (2016a). USGS FAQ. Retrieved from www.usgs.gov/faq

U.S. Geological Survey. (2016b). Water data for the nation. Retrieved from <https://waterdata.usgs.gov/nwis>

Vermeer, M., & Rahmstorf, S. (2009). Global sea level linked to global temperature. *Proceedings of the National Academy of Sciences* 106, 21527–21532.

Walton, T. L. (2007). Projected sea-level rise in Florida. *Ocean Engineering* 34, 1832–1840.

Warren, R. S., & Niering, W. A. (1993). Vegetation change on a northeast tidal marsh: interaction of sea-level rise and marsh accretion. *Ecology* 74, 96–103.

Wilmott, C. J., Robeson, S. M., & Matsuura, K. (2012). A refined index of model performance. *International Journal of Climatology* 32, 2088–2094.

Wiseman, W. J., Swenson, E. M., & Power, J. (1990). Salinity trends in Louisiana estuaries. *Estuaries* 13, 265–27

VITA

Personal Information

Name: Teddy Mujinga Mulamba



Citizenship: South African

Marital Status: Single

Children: None

Education

- B.Sc., Civil Engineering, 2014, University of North Florida, Jacksonville, Florida

Honors and Awards

- Taylor Engineering Research Institute Scholarship 2015-2016
- University of North Florida Dean's List Spring 2013, 2014
- University of North Florida Student-Athlete Advisory Committee, Vice President (Fall 2012- Fall 2014)
- University of North Florida NCAA Division 1 Mens Soccer Captain (Fall 2011- Fall 2014)
- Atlantic Sun Conference All-Academic Student Athlete

Association Memberships

- National Society of Black Engineers (NSBE)
- Ocean, Ports and Rivers Institute (COPRI)
- American Society of Civil Engineers (ASCE)

Professional Experience

University of North Florida, Jacksonville, Florida

- Graduate Research Assistant (Spring 2015- Present)

CSI GEO, Inc.

- Geotechnical Engineering Intern (Spring- Summer 2014)

INTERA Inc.

- Coastal Engineering Intern (Summer 2016- Present)